MICRO-3D SCULPTURED METASTRUCTURES

A THESIS SUBMITTED TO
THE GRADUATE SCHOOL OF ENGINEERING AND SCIENCE
OF BILKENT UNIVERSITY
IN PARTIAL FULFILLMENT OF THE REQUIREMENTS FOR
THE DEGREE OF
MASTER OF SCIENCE
IN
ELECTRICAL AND ELECTRONICS ENGINEERING

By
Anıl Çağrı Atak
June 2023

MICRO-3D SCULPTURED METASTRUCTURES
By Anıl Çağrı Atak
June 2023

We certify that we have read this thesis and that in our opinion it is fully adequate, in scope and in quality, as a thesis for the degree of Master of Science.

Hilmi Volkan Demir(Advisor)

Erdinç Tatar

Nihan Kosku Perkgöz

Approved for the Graduate School of Engineering and Science:

Orhan Arıkan
Director of the Graduate School

ABSTRACT

MICRO-3D SCULPTURED METASTRUCTURES

Anıl Çağrı Atak
M.S. in ELECTRICAL AND ELECTRONICS ENGINEERING
Advisor: Hilmi Volkan Demir
June 2023

Today three-dimensional (3D) printers are highly popular and find use in a vast range of applications thanks to their capability to construct complex 3D structures. However, 3D-printing vertical structures with a high aspect ratio of height to width remains a pending challenge especially when a high lateral resolution is required in large footprints. In this thesis, we propose and demonstrate micro-3D sculptured metastructures using the idea of constructing deep trenches to erect their high aspect ratio metal lines along long strips. To generate such deep-trenched 3D-patterns, our construction relies on nonlinear absorption process, enabling the two-photon polymerization (2PP). In our fabrication, the 2PP process requires optical trajectory optimization, followed by electroplating thick metal film and dry etching seed layer. To test the developed process flow of 2PP, we built three-dimensional RF metastructures showcasing the depth effect as a third dimension. Based on our systematic numerical and experimental studies, our designed metastructure resonators are found to fall within a targeted specific operating resonance frequency range, with their resonance frequency being controlled and shifted and their quality factor (Q-factor) tuned as a function of their cross-sectional aspect ratio. In the thesis, with these proof-of-concept demonstrations, we show that such 2PP-defined high aspect ratio RF resonators highly benefit in terms of tunability of their resonance frequencies, along with increased Q-factor and reduced footprint. The findings of this thesis indicate that the proposed fabrication method of producing deep trenches via 3D-printing provides rich opportunities to implement high aspect ratio, complex structures that are highly miniaturized.

Keywords: Deep trenches, three-dimensional printing, two-photon polymerization, electroplating, RF metastructures, RF resonators.

ÖZET

MİKRO-3D ŞEKİLLENDİRİLMİŞ METAYAPILAR

Anıl Çağrı Atak
Elektrik Elektronik Mühendisliği, Yüksek Lisans
Tez Danışmanı: Hilmi Volkan Demir
Haziran 2023

Günümüzde üç-boyutlu (3B) yazıcılar oldukça popülerdir ve karmaşık 3B yapılar oluşturma yetenekleri sayesinde çok çeşitli uygulamalarda kullanım alanı bulmaktadır. Fakat, yüksek boy-en oranına sahip dikey yapıların 3B yazdırılması, özellikle büyük taban alanlarında yüksek yanal çözünürlük gerektiğinden dolayı çözümlenmemiş bir zorluk teşkil etmeyi sürdürmektedir. Bu tezde, yüksek boy-en oranına sahip metal hatlar inşa etmek için derin yarıklar oluşturma fikrini kullanarak mikro-3B şekillendirilmiş metayapıları önermekte ve göstermekteyiz. Bu tür derin yarıklı 3B-tasarımlar oluşturmak için inşamız iki-foton polimerizasyonunu mümkün kılan doğrusal olmayan soğurma işlemine dayanmaktadır. Üretim sürecimizde, iki-foton polimerizasyon işlemi için optik yörünge optimizasyonu, bu işlemi takiben de elektroliz yöntemiyle kalın metal film kaplanması ve kaplamada kullanılan iletken tabakanın kuru aşındırılması gereklidir. İki-foton polimerizasyonunun geliştirilmiş süreç akışını test etmek amacıyla, derinlik etkisini üçüncü bir boyut olarak gösteren 3B radyo frekansı (RF) metayapılarını oluşturduk. Sistematik sayısal ve deneysel çalışmalarımıza dayanarak tasarlanmış metayapı rezonatörlerimizin kesitsel boy-en oranlarının fonksiyonu olarak kontrol edilip kaydırılan rezonans frekansları ve ayarlanan kalite faktörü ile hedeflendiği gibi belirli bir çalışma rezonans frekans aralığına düşmesi sağlanmıştır. Tezde yüksek boy-en oranlı metayapıların kavramsal olarak gösterimleri aracılığıyla, bu tür iki-foton polarizasyon tanımlı yüksek boy-en oranlı RF rezonatörlerin arttırılmış kalite faktörü ve azaltılmış taban alanıyla beraber rezonans frekanslarının ayarlanabilirliği açısından büyük fayda sağladığını gösterilmiştir. Bu tezin bulguları, 3B yazım yoluyla derin yarıklar üretmek için önerilen fabrikasyon yönteminin, oldukça minyatürleştirilmiş karmaşık yapıları uygulamak adına zengin fırsatlar sağladığını işaret etmektedir.

Anahtar sözcükler: Derin yarıklar, üç-boyutlu baskı, iki-foton polimerizasyon, elektroliz yöntemiyle kaplama, RF metayapılar, RF rezonatörler.

Acknowledgement

First, I would like to thank Prof. Hilmi Volkan Demir for supervising, directing and helping me during my research. I learned a lot from him about research and academic life. Undoubtedly, it is a great honor to graduate as his student.

I also would like to thank my thesis committee members Asst. Prof. Erdinç Tatar and Prof. Nihan Kosku Perkgöz for their interest in my thesis.

I would like to thank Emre Ünal, Furkan Şahin, and Tuğba Karahan Kılıç for their help during my research. Also, I would like to thank all the members of the Demir Research group, Özgün Akyüz, Rabia Önen, Dr. Savaş Delikanlı, Dr. Betül Canımkurbey, Dr. Zeynep Dikmen, Farzan Shabani, Furkan Işık, Aziz Taner Astarlıoğlu, Rumon Miah, Taha Haddadi, İklim Yurdakul, Taylan Bozkaya, Ahmet Tarık Işık, Mohsin Waris, İlayda Özkan, Sobhan Gholami, and Tevfik Bülent Kanmaz. We have always had a very friendly atmosphere in our group. Therefore, I present my gratitude to all of them.

I would like to express my endless gratitude to my mother Füsun, my father Nafi, my sisters Burcu, Başak, and Bahar. Finally, my deepest gratitude goes to my love Ecenaz who has always supported me tremendously ...

Contents

1 Introduction **1**

1.1 Motivation and Objectives 1

1.2 Thesis Outline 2

2 Scientific Background **4**

2.1 Two-Photon Polymerization (2PP) 4

2.2 Metamaterials 8

3 Designing our RF Metastructures **12**

3.1 Analytical and Numerical Solutions for our RF Metastructures . . 13

3.2 Simulating Microstrip Ring 23

3.3 Stimulating Experimental Setup 25

4 Fabrication of our High Aspect Ratio RF Metastructures **29**

4.1 Two-Photon Polymerization 31

4.2 Copper Electroplating 37

4.3 Seed Layer Etching 44

5 Proof-of-Concept Demonstration of our High Aspect RF Metastructures 47

5.1 Our Experimental Measurement Setup 48

5.2 Imagining our Fabricated RF Metastructure Resonators 50

5.3 Testing and Analyzing our RF Metastructure Resonators 52

5.3.1 Resonance Frequency and Q-factor 52

5.3.2 Miniaturization 57

6 Conclusion and Outlook 60

List of Figures

2.1 Illustration of one-photon and two-photon absorption based excitations. 6

2.2 Materials categorization with respect to permittivity and permeability. 9

3.1 Our numerical simulation setup 1 with its boundary conditions. . 14

3.2 Our numerical simulation setup 2 with its boundary conditions. . 15

3.3 Numerical results using simulation setup 1 parametrized with respect to systematically varied cross-sectional aspect ratios (from AR=0.33 to AR=40) by changing the metal thickness from 1 to 120 µm while keeping the width (3 µm) and the gap (1200 µm) fixed. 17

3.4 Q-factor as a function of aspect ratios numerically computed using simulation setup 1 by changing metal thickness. 18

3.5 Numerical results using simulation setup 2 parametrized with respect to systematically varied cross-sectional aspect ratios (from AR=0.33 to AR=40) by changing the metal thickness from 1 to 120 µm while keeping the width (3 µm) and the gap (1200 µm) fixed. 19

3.6 Q-factor as a function of aspect ratios numerically computed using simulation setup 2 by changing metal thickness. 20

3.7 Numerical results using simulation setup 1 parametrized with respect to systematically varied metal thickness (from TH=3 µm to TH=120 µm) while keeping the width (600 µm) and the gap (30 µm) fixed. 21

3.8 Numerical results using simulation setup 2 parametrized with respect to systematically varied metal thickness (from TH=1 µm to TH=6000 µm) while keeping the width (600 µm) and the gap (30 µm) fixed. 22

3.9 Microstrip ring: (a) microstrip ring with the feed line and (b) its zooming along with the dimensions for the microstrip ring geometrical parameters. 23

3.10 Electric field map of the microstrip ring. 24

3.11 Numerical analysis for the microstrip ring and the glass over the microstrip ring. 25

3.12 Numerical simulation of the experimental setup with our RF metastructure resonator on it. 26

3.13 Electric field distribution of the experimental setup with our RF metastructure resonator on it. 26

3.14 Numerical simulation for the aspect ratio effect for our RF metastructure using the microstrip ring. 27

4.1 Proposed process flow. The developed fabrication methods consist of the following steps: (a) Spin-coated AZ-4562 positive photoresist over ITO-coated glass, (b) placing the prepared substrate on the sample holder of the 3D printing system and exposing light to obtain the desired pattern, (c) developing the exposed part of the photoresist, (d) thick film deposition of copper metal over ITO seed layer along the line of the given pattern, (e) spin-coated the protecting layer, (f) cutting the substrate into smaller pieces with a dicing saw, (g) removing the photoresist, (h) dry etching of the ITO seed layer with ICP, and (i) thermal annealing to strengthen copper structure. 30

4.2 The Microlight3D Printer based on 2PP and its general mechanism. 31

4.3 Computation of the laser trajectories. 33

4.4 Computation of the laser trajectory with (a) slicing, (b) the lines filling the interior, and (c) in combination. 34

4.5 Hatching effect on the laser trajectory with green horizontal lines. 35

4.6 Adjusting focal point by changing z-axis. The first focal point (a) shows the interface between air and resin, and the second focal point (b) shows the interface between resin and substrate. 36

4.7 High aspect ratio design pattern with (a) 10-11 µm deep third-dimension and 2-3 µm width and (b) flat sidewalls. (Scale bars: 5 and 10 µm, respectively). 37

4.8 Schematic of our electroplating setup. 38

4.9 A small area of the photoresist removed from the sample to prepare it for electroplating. 39

4.10 Our electroplating setup. 40

4.11 Deposition uniformity difference of high current density (a) and low current density (b). (Scale bars: 30 and 5 µm, respectively). . 41

4.12 Improved uniformity with customized current signal using both forward pulse and reverse pulse for the plated parts (a), over-plating and under-plating problems in some local parts before removing the photoresist (b). (Scale bars: 10 and 100 µm, respectively). . . 42

4.13 Stirrer effect when using along with the customized current source. (Scale bar: 30 µm). 42

4.14 Uniform metal deposition when using current controlled voltage source after removing photoresist. (Scale bar: 10 µm). 43

4.15 Etching processes. 45

4.16 Seed layer etching mechanism for our RF metastructure resonator. 46

5.1 Our home-built microstrip ring setup: (a) frontside of the microstrip ring and (b) backside of the microstrip ring. 48

5.2 S_{11} of the microstrip ring with and without a glass substrate. . . . 49

5.3 Our fabricated RF metastructure resonator using the proposed process flow: (a) Red lines show the metal parts, while dark parts show the glass, (b) zoomed at the corner and (c) with the physical dimensions of the metastructure which are T:4-6 µm, W:2-3 µm, L:4.3 mm, G:1.2 mm. (Scale bars: 2 µm and 1 mm, respectively). 50

5.4 Scanning electron microscopy images of our fabricated RF metastructures, shown with the aspect ratios of the metal parts, which are 1, 2, and 4, respectively. (Scale bars: 10 µm and 300 µm, respectively). 51

5.5 S_{11} spectra: (a) Numerical simulation results and (b) experimental measurement result. The resonance frequency and Q-factor increase with the increasing metal thickness while keeping metal width fixed. 53

5.6 Numerical analyses for the capacitance as a function of the metal thickness. 54

5.7 Numerical analyses for inductance as a function of the metal thickness. 55

5.8 Numerical analyses for resonance frequency as a function of the metal thickness. 56

5.9 Conventional RF metamaterial resonator fabricated by the PCB milling and prototyping machine. (Scale bar: 1 mm). 57

5.10 Our high-aspect ratio resonator fabricated by our proposed fabrication methods with 2PP. (Scale bar: 1 mm). 58

5.11 S_{11} spectra experimentally measured and numerically calculated for (a) the RF metastructure resonator fabricated by the PCB LPKF machine and (b) our RF metastructure resonator fabricated by our proposed method. These result show that the length of the resonator decreases from 5.8 mm to 4.3 mm, and the metal width decreases from 0.6 mm to sub-10 µm while increasing the aspect ratio to keep the same resonance frequency range and quality factor. 59

Chapter 1

Introduction

1.1 Motivation and Objectives

Three-dimensional (3D) printers have gained popularity globally owing to their capabilities for implementing complex structures. However, 3D-printing vertical structures with a high aspect ratio remains a pending challenge, especially when a high lateral resolution is required in large footprints. Two-photon polymerization (2PP), based on a nonlinear optical absorption for the chemical reaction of the focused region inside a photoactive polymer is one of the most prominent technologies in those 3D printing systems. This process, enabling the adaptation of various methodologies to fulfill specific demands and technical requirements, facilitates the design of 3D patterns with high accuracy and offers the possibility to create high aspect ratio designs.

It is well known that RF metamaterials have been utilized in many applications including sensing and material characterization. However, there are some limitations regarding the patterning capability and resolution when conventional methods of printed circuit board (PCB) machines and other lithography techniques are used in the fabrication of RF metamaterials. Thus, RF metastructures

showcasing the depth effect as the third dimension are good candidates for testing a proposed process flow including 3D-printing system. Besides, the numerical computations predict that deep trenches in RF structures may be beneficial to miniaturizing metal footprint size, increasing the quality factor, and tuning the resonance frequency.

To the best of our knowledge, there is no developed process flow for RF metastructures using micro-3D-sculptured deep trenches. In this thesis, we proposed and developed a fabrication approach, along with its specific process flow relying on 3D-printing technology for RF metastructures. We built our micro-3D sculptured high aspect ratio deep trenches with the help of 2PP. Also, we integrated the constructed 3D patterns with electroplating for thick metal film deposition, dry etching to remove the seed layer, and rapid thermal annealing to obtain higher conductivity in our construction. Here, we applied this fabrication process flow to a new class of metastructures that consist of customized resonators in the resonance frequency range of 4 - 6 GHz. Leveraging on the developed process flow, we achieved the miniaturization of metal footprints and tuning of the resonance frequency with increasing quality factor. Our findings indicate that this process flow provides rich opportunities to implement high aspect ratio and complex structures.

1.2 Thesis Outline

In Chapter 2, two-photon polymerization methods and metamaterials, two main topics of the thesis, are reviewed and described with introductive information. Chapter 3 presents the design process and aspect ratio analysis of RF metastructures, showing the depth effect by using the third dimension, with numerical solutions before moving to the fabrication part. Chapter 4 discusses the steps of the proposed fabrication with the entire process flow for RF metastructures. Here, we describe step by step the 2PP to implement micro-3D sculptured deep trenches for the RF pattern, electroplating for copper deposition, and dry etching of indium tin oxide (ITO) seed layer. Chapter 5 covers the results of RF

structures with their SEM imaging and their RF measurements using a network analyzer. Last, Chapter 6 concludes with a summary of the fabrication process flow and proof-of-concept model and discusses their advantages, future prospects.

Chapter 2

Scientific Background

2.1 Two-Photon Polymerization (2PP)

The phenomenon of two-photon processes emerged with Maria Goeppert-Mayer's pioneering work [1]. In her work, this groundbreaking idea was based on that two-photon absorption (2PA) takes place through virtual states of the materials. A virtual energy state can be created when the molecule absorbs a photon. Two-photon absorption occurs when a second photon is absorbed while this virtual state is still present. In contrast to the typical single-photon excitation requiring only one photon, two-photon absorption modifies the energy state of the absorbing molecule by using multiple photons at a longer wavelength. After Mayer's early idea about the two-photon process, the scope of conventional two-dimensional (2D) microfabrication approaches has been expanded to include third-dimension capability. An experimental microfabrication in 1997 was created using a Ti:sapphire laser with a pulse width of 200 fs at a wavelength of 790 nm. Here, the first 3D micro-fabricated structures were obtained experimentally with the stimulation of two-photon absorption. This initiated the emergence of a new 3D-printing technology [2].

This new technology utilized for microfabrication is two-photon polymerization

(2PP), relying on nonlinear two-photon optical absorption to induce the chemical reaction in the focused region of the photoactive polymer. Although some previous studies used electron beams, optical and nanoimprinting lithography techniques used in nanophotonic, microelectronic, microfluidic, and biomedical domains suffer the limitations of having high aspect ratio structures, limited material selection and resolution, high cost, or lack of 3D capability. Such limitations can inhibit desired applications.

On the other hand, 2PP is a powerful technique to overcome the fabrication difficulties of complex structures providing new design options that are otherwise impossible with other methods but possible with this method using the layer-by-layer method. The 2PP technique allows for the implementation of 3D surfaces, while providing high accuracy and a small feature size (potentially below 100 nm) [3] with relatively short fabrication time.

To understand the mechanism of 2PP technique, we can first analyze the photo-polymerization, having three parts: initiation, propagation, and termination processes. When we look at the initiation part, photo-initiators generate the excited state upon the optical absorption of two photons $hv + hv$ and decompose into radicals (R.) [3]:

$$PI \rightarrow PI^* \rightarrow R. + R. \tag{2.1}$$

Moreover, the optimization of commercial photo-initiators makes a major research effort and those previous studies have created newly available photo-initiators for the use in 2PP [4]. In the propagation process, monomers (M) integrate with radicals:

$$R. + M \rightarrow RM. \rightarrow RMM. ... \rightarrow RM_n. \tag{2.2}$$

In the termination process, two monomer radicals are integrated with each other:

$$RM_n. + RM_m. \rightarrow RM_{n+m}R. \tag{2.3}$$

There is a fundamental difference between 1PA and 2PA. The aforementioned photo-initiators absorb two photons simultaneously during the transition from a lower energy state to a higher energy state. Here, the subtraction of the two energy levels is the same with the total energy of two photon together. The

absorption rate, which is proportional to the square of light intensity, is given in terms of the intensity of the incident light (I), refractive index (n) of the medium, speed of light in vacuum (c), the optical frequency of the incident light (ω) , and imaginary part of the third-order susceptibility light (φ^3) of the medium [6-7], which is the imaginary part of the comprehensive evaluation of nonlinear optical effects in a medium that exhibit dependency on the third power of the electric field of the incident monochromatic beam as follows [3,5]:

$$\frac{dW}{dt} = \frac{8\pi^2\omega}{n^2c^2} \cdot I^2 Im(\varphi^3) \tag{2.4}$$

When the radical concentration exceeds the threshold level, polymerization starts. To comprehend the 2PP mechanism, the general mechanism is illustrated in Figure 2.1.

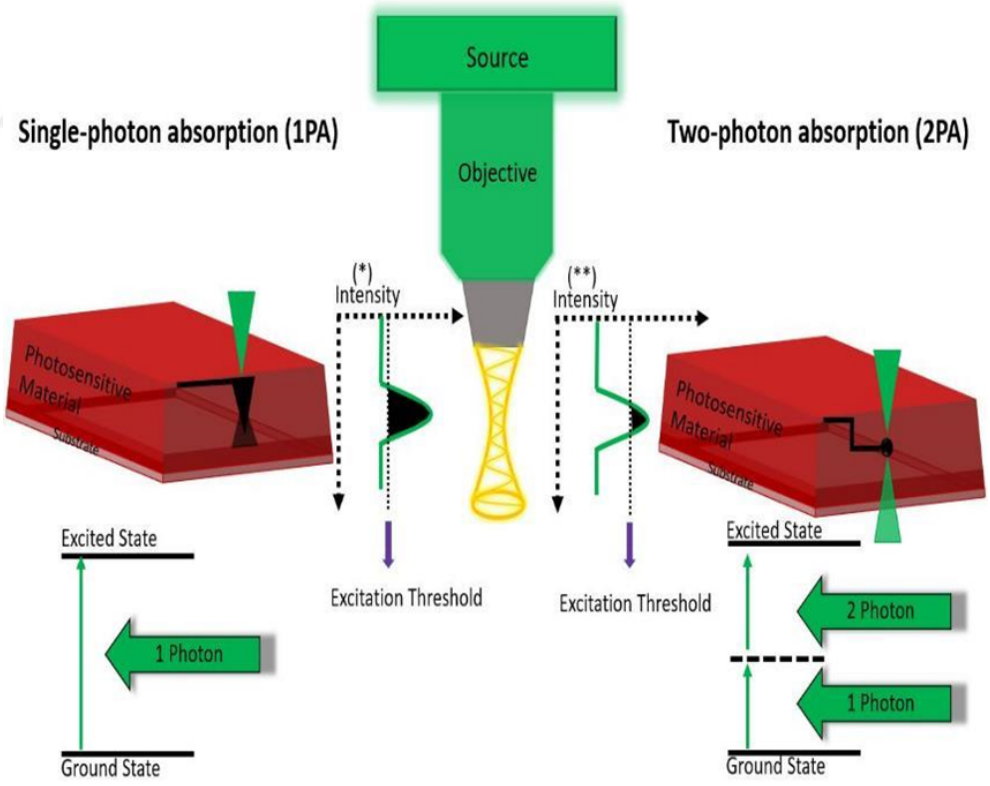

Figure 2.1: Illustration of one-photon and two-photon absorption based excitations.

The 2PP offers several advantages over the one-photon case. One of the advantages is that the laser light goes deeper into photosensitive material to induce

polymerization without affecting the outside of the focal region. The other advantage is that the polymerization rate on the light intensity has quadratic dependence and provides an improved spatial resolution with higher accuracy. Figure 2.1 also illustrates the difference between the single-photon and two-photon absorption-based mechanisms. In the two-photon excitation case, polymerization occurs within a limited volume region where the intensity squared in a transverse cross-section of the beam is above the threshold to provide sufficient absorption for the chemical reaction [8]. Therefore, this technique is based on the nonlinear optical absorption of a firmly focused laser beam for crosslinking in a small volume (voxel) of a photosensitive material. As an important advantage, we can adjust the path along which 3D shapes are formed while moving the focused volume region (focal point) inside photosensitive material.

Today as a result of this capability, 2PP finds use in a wide range of applications [9], including preparation of plasmonic structures [10], helical photonic structures [11], microfluidic channels [12], and micro-electromechanical systems [13].

The versatility of this 3D printing technique allows for a diversity of application areas. Its high capability enables the adaptation of various methodologies to fulfill specific needs and requirements; for example, having high aspect ratio features is a challenging demand [14]. Other conventional lithography techniques, such as electron beam lithography (EBL), nanoimprinting lithography (NIL) and optical lithography, can provide an opportunity for the fabrication of high aspect ratio structures with undesired limitations. Even the choice of photoresist used in these lithography techniques is critical, as removing negative photoresists can be challenging without the use of additional chemicals or etching technology. In addition, forming high aspect ratio metal structures through metal deposition following the lithography process is severely limited in terms of the total thickness of the resulting metal structure, workable footprint, and patterning capability. The EBL method can produce high aspect ratio structures [15-21] with limited total thickness and footprint. While the high aspect ratio metal patterns existed in only some of these previous studies [19-21], even an aspect ratio of 1:1 is technically problematic in micrometer ranges because it is not possible to make structures with vertical dimensions thicker than 2 µm. The NIL technique yielded

an aspect ratio of around 4, but the total thickness remains unchanged up to 2 micrometers [22-23]. Regarding optical lithography, it is apparent that the overall thickness is more remarkable than both EBL and NIL [24-25]. However, sidewalls are not perpendicular to the plane, caused by the proximity effect. Moreover, 2PP, having a wider range of material selection possibilities, the nonrequirement of the utilization of a hard mask or a mold, and cost-effectiveness set itself apart from conventional lithography techniques that require specialized equipment such as electron beam or high vacuum systems. Therefore, these conditions make 2PP a more economical choice. Additionally, 2PP consequentially helps to construct 3D patterns, which is impossible to implement with other lithography techniques.

2.2 Metamaterials

The term metamaterial consists of two parts: meta and materials. The meaning of meta is "beyond" and comes from Greek, and then the meaning of metamaterial is intended to imply different properties beyond the natural materials. There are two fundamental electromagnetic properties, permittivity (ε) and permeability (μ) of a medium, which contribute to characterizing electric and magnetic fields in different media, respectively. Quantifying a material's ability to store electrical energy is possible through the permittivity, and a material's ability to store magnetic energy, through permeability.

Metamaterials are artificial materials having unique electromagnetic properties produced by engineering the permittivity and permeability. Theoretically, Veselago first predicted a metamaterial concurrently with negative permittivity and negative permeability in 1968 [26]. Later, Pendry reported left-handed materials (LHMs) in 1999 [27]. When a monochromatic plane wave propagates in an isotropic and homogenous medium, the electric field and magnetic field wave vectors form as a right-handed triplet vector with the direction of wave propagation in a medium of positive permittivity and permeability. However, they are left-handed triplets when the permittivity and permeability are negative, and the refractive index must have a negative sign. LHMs are an example of such

negative index materials.

In Figure 2.2, there is a chart for the properties of the materials corresponding to their electromagnetic properties to classify metamaterials. The region in this chart having $\varepsilon > 0$ and $\mu < 0$ covers some ferrites materials, and the region in the chart having $\varepsilon < 0$ and $\mu > 0$ covers metals and semiconductors. Furthermore, the region with $\varepsilon > 0$ and $\mu > 0$ is the region of right-handed materials and covers most dielectric materials. There are no materials with negative permittivity and negative permeability (or thus negative refractive index) in natural materials, corresponding to the region of left-handed medium in the chart with $\varepsilon < 0$ and $\mu < 0$ covering the metamaterials. After approximately three decades since Veselago's prediction, the experimental realization of negative refractive index materials was achieved by Smith et al [28]. The combination of previous theoretical suggestions regarding metamaterials and their possible applications was based on Pendry's proposal of split ring resonators (SRRs) [29].

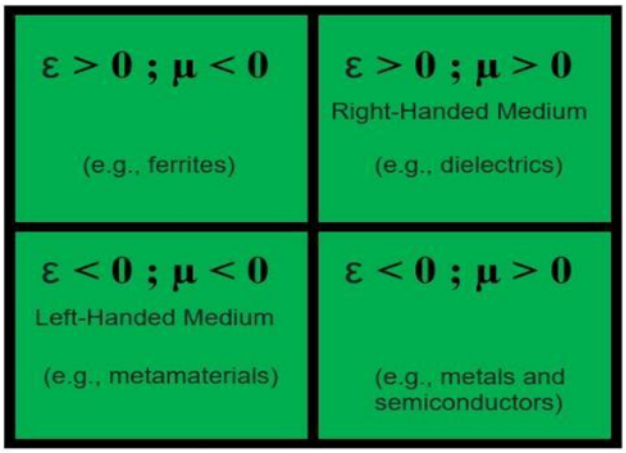

Figure 2.2: Materials categorization with respect to permittivity and permeability.

Characteristic features of metamaterials with both negative permittivity and permeability properties have enabled their use in a wide range of disciplines such as material science, physics, engineering, and many other scientific fields. Photonic metamaterials refer to the materials intentionally designed to demonstrate a tailored electromagnetic response at the light frequencies. Those materials are

made to manipulate light in controllable ways that are impossible with natural materials [30]. The working areas of optical metamaterials include optical magnetism and optical negative refraction, chirality, and nonlinear optics [30]. As a more general class, electromagnetic metamaterials refer to the artificially created composite materials that interact with electromagnetic waves, such as radio frequency (RF), microwave, and optical waves, in unique ways that are not conceivable with standard materials [31].

Mechanical metamaterials are artificially engineered materials designed to import efficient and remarkable mechanical properties, e.g., elastic mechanical properties of linear and nonlinear behaviors. Those metamaterials exhibit zero or negative values for conventionally positive mechanical parameters such as Poisson's ratio and modulus [32].

RF metamaterials, also alternatively referred to as electromagnetic metamaterials as a more general class, have been used in many places, such as sensing [33], material characterization [34], and device miniaturization [35]. Their quality factor, miniaturization capacity, and resonance frequency tunability are essential aspects in those applications. The quality factor (Q-factor) is a figure of merit to determine the resonance performance (sharpness of the resonant) [36]. The higher Q-factor leads to a higher sensor performance with enhanced sensitivity in the case of using a resonant sensing metamaterial. Miniaturization diminishes a RF structure's dimensions, lowering its cost [37]. In addition, it is crucial to consider the resonance frequency of a RF resonator, as well as the effect of geometrical factors on its resonance frequency shift. These factors play an essential role in determining the operating range of a RF resonator. In recent years, studies have been taking into account the effect of finite conductive thickness of a RF resonator [38-40] to tune its resonance frequency. Therefore, careful consideration and analyses of these factors with the fabrication process flow are necessary to ensure the reliable, efficient operation of such a RF resonator. However, their fabrication methods are limited when well-known fabrication techniques, such as printed circuit board (PCB) technology, optical lithography, and electron beam lithography (EBL), are considered. Those conventional methods suffer problems in terms of patterning capability and resolution, limiting such RF structures'

designs.

In this thesis work, we have investigated alternative process flows and electromagnetically tested their resulting devices. Here, our proposed fabrication approach is a powerful candidate to overcome these issues by demonstrating our fabrication steps of a proof-of-concept demonstration RF model. Furthermore, adding new capabilities to our fabrication provided an improved quality factor, increased miniaturization, and widely tuned resonance frequency as important advantages.

Chapter 3

Designing our RF Metastructures

This chapter is based on our manuscript prepared by *Anıl Çağrı Atak, Emre Ünal, and Hilmi Volkan Demir*, which is in submission (2023).

In this thesis, our main aim is to develop and demonstrate our fabrication process flow that is based on constructing micro-3D-sculptured deep trenches, electroplating for thick metal film deposition and dry etching to remove the seed layer to implement the design of our RF metastructures. For this reason, we chose our proof-of-concept demonstration model to be high aspect ratio RF metastructures that apply the third-dimension effect to well-known two-dimensional RF metamaterials with sub-10 µm resolution. The idea of RF metastructure comes with the concept of SRRs, well-known RF metamaterials, including one or more metallic rings with a split. These resonators are excellent candidates for transition from planar to 3D designs with the extrusion of vertical dimension. To this end, we selected this class type of RF metastructures as the test model also to demonstrate the importance of high aspect ratio metal partials, generally ignored, in analyzing SRRs. In designing our RF resonators, we numerically simulated metastructures using full electromagnetic solutions (CST Microwave Studio). Their resonance frequencies were intended to be placed in a targeted frequency range while undertaking comparative analyses concerning the resonance frequency shift, Q-factor, and overall footprint size as a function of their

cross-sectional aspect ratios. Furthermore, resonance characterization of our resonators is required, and we selected a microstrip ring architecture as an antenna to experimentally perform their measurements.

In this chapter, Section 3.1 explains analytical and numerical analyses of our RF designs with varied cross-sectional aspect ratios. Sections 3.2 and 3.3 discuss the basics of the microstrip ring and the combination of our RF structures with the microstrip ring to be used in our experimental setup in the next chapter.

3.1 Analytical and Numerical Solutions for our RF Metastructures

We used the frequency domain solver in CST microwave studio utilizing tetrahedral meshing for design process and numerical analyses of our RF metastructure resonators. In this procedure, geometrical dimensions of the resonators including the metal width and thickness, the total length, and the split were set and tuned to obtain the resonance frequency targeted to fall in the desired frequency range of 4 - 6 GHz. In these simulations, the resonator substrate differs from conventional methods. Although the substrate in PCB-based designs is typically FR-4 or Rogers, here we used 1.1 mm thick glass being completely transparent in the visible range with an approximate dielectric constant of 6 to apply our process flow. After adjusting the dimensions and substrate specification of our resonators, boundary conditions and excitations were all defined to match our experimental setting as well.

Implementing our simulation setup, the appropriate boundary conditions of a perfect electric conductor (PEC) and a perfect magnetic conductor (PMC) in open space is essential to observe resonances [41]. The PEC condition enforces zero tangential components of the electric field, the PMC condition dictates zero tangential components of the magnetic field, and the open condition provides an extension of the geometry. In the boundary condition selection for our case, it

is crucial that electric and magnetic fields should be orthogonal [41]. Also, they are perpendicular to the propagation direction. For excitation, waveguide ports, where our structure is placed for electromagnetic waves to enter and leave, were used. In Figure 3.1, the direction of the electromagnetic wave propagation is given through the x-axis. The electric and magnetic fields are along the y-axis and z-axis, respectively.

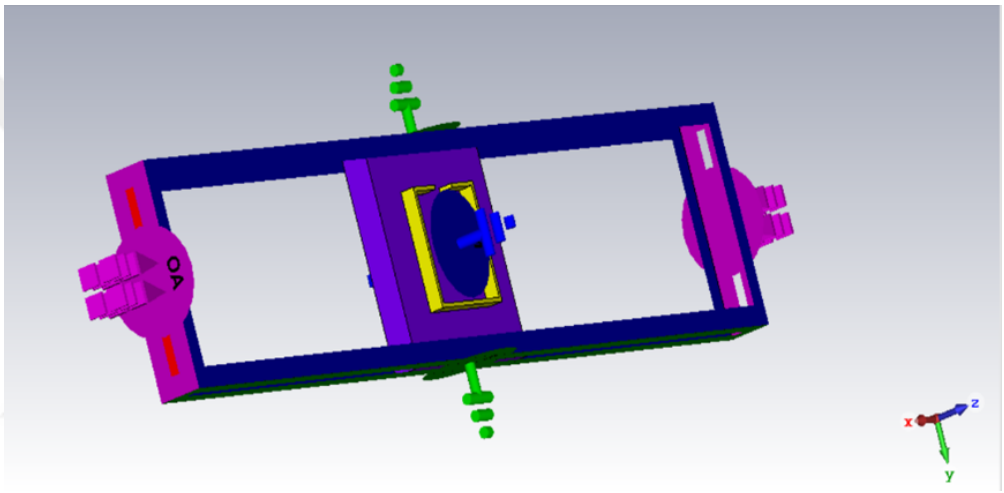

Figure 3.1: Our numerical simulation setup 1 with its boundary conditions.

In Figure 3.2, the electromagnetic wave propagates in the z-direction. The electric and magnetic fields are along the x- and y-axes, respectively. In these simulation setups, the one-side length of our RF structure is 4.3 mm. The metal thickness is varied from 1 and 120 µm while the width takes only two distinct values, which are 3 and 600 µm, to analyze the cross-sectional aspect ratio effect in the structures. The gap also has two different values, 1200 and 30 µm. We chose two different dimensions both for the width and gap to observe the frequency shift as a result of the aspect ratio effect in the different possible operation states of capacitive and inductive dominance.

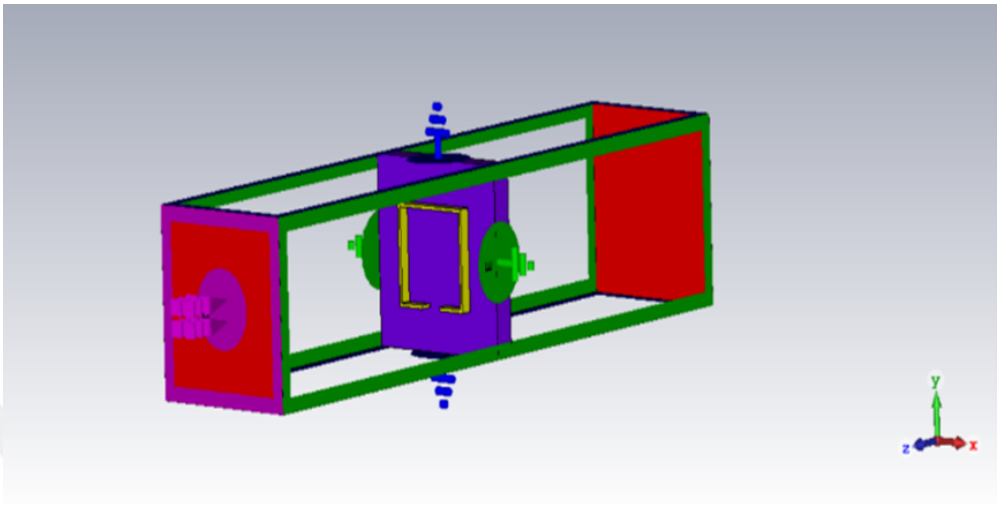

Figure 3.2: Our numerical simulation setup 2 with its boundary conditions.

It is seen that there is a considerable length difference between the shortest part and the longest part of the structure. Thus, adjustments such as setting the threshold value for meshing in the simulation tool are essential to obtain correct results. Based on a finite element model for solving Maxwell's equations, the frequency domain solver with adaptive tetrahedral meshing was utilized to run the simulation within the desired frequency range (4 – 6 GHz). Through simulation, we obtained the S-parameters of the structures that help to characterize the relationship of the incident wave pinging on the structure's ports to those reflected and transmitted from them. The S-parameter spectra gives information about the resonance frequency and Q-factor of the metastructure resonators allowing to make comparative analysis using systematically varied geometrical parameters. Here, the structure's equivalent circuit model and the analytical approach based on it are useful to comprehend the simulation results parametrized with respect to geometrical variations.

The resonance frequency can be calculated using the following geometrical parameters based on LC equivalent circuit model [38-40]:

$$f_{res} = \frac{1}{2\pi\sqrt{L_{total} \times C_{total}}} \tag{3.1}$$

$$L_{total} = (1 - \frac{g}{4l}) \times \mu_0 \times \frac{1}{\pi} \times [2l \times \ln \frac{2l^2}{w \times t} - 2l \times \ln (l(1 + \sqrt{2})) \\ -l + 2l\sqrt{2} + 0.447(w + t)] \tag{3.2}$$

$$C_{total} = \frac{\varepsilon_0 \varepsilon_{\mathrm{g}}(t \times w)}{g} + \varepsilon_0 \varepsilon_{\mathrm{g}}(t + g + w) + 2(t + w) \times \varepsilon_{\mathrm{s}} \times C_{surf}^{pul} \tag{3.3}$$

$$C_{surf}^{pul} = \int_I^J \frac{\sigma \times ds}{V} \tag{3.4}$$

where

ε_0: free-space permittivity

ε_{g}: effective dielectric constant for substrate

ε_{s}: effective dielectric constant for metal ring

μ_0: free-space permeability

t: metal thickness

w: metal width

g: split-gap of the resonator

l: length

C_{surf}^{pul}: surface capacitance per unit length

σ: surface charge density

ds: integral element of length (differential length) of the loop

V: potential difference between opposite points of the loop

As mentioned above, the varied geometric dimensions were set in all parts and applied to analyze and understand the importance of the cross-sectional aspect ratio in the resonance behavior.

The Q-factor can be calculated using the 3 dB difference spectral points ($f_{max_{3dB}} - f_{min_{3dB}}$) around the resonance frequency ($f_{resonance}$):

$$Q - factor = \frac{f_{resonance}}{(f_{max_{3dB}} - f_{min_{3dB}})} \tag{3.5}$$

In Figure 3.3, while the side length of the resonator was fixed at 4.3 mm, the width at 3 µm, and the gap at 1200 µm, the metal thickness was increased from 1 to 120 µm in a systematic manner. The Q-factor is observed to increase with the increasing aspect ratio (AR), also depicted in Figure 3.4.

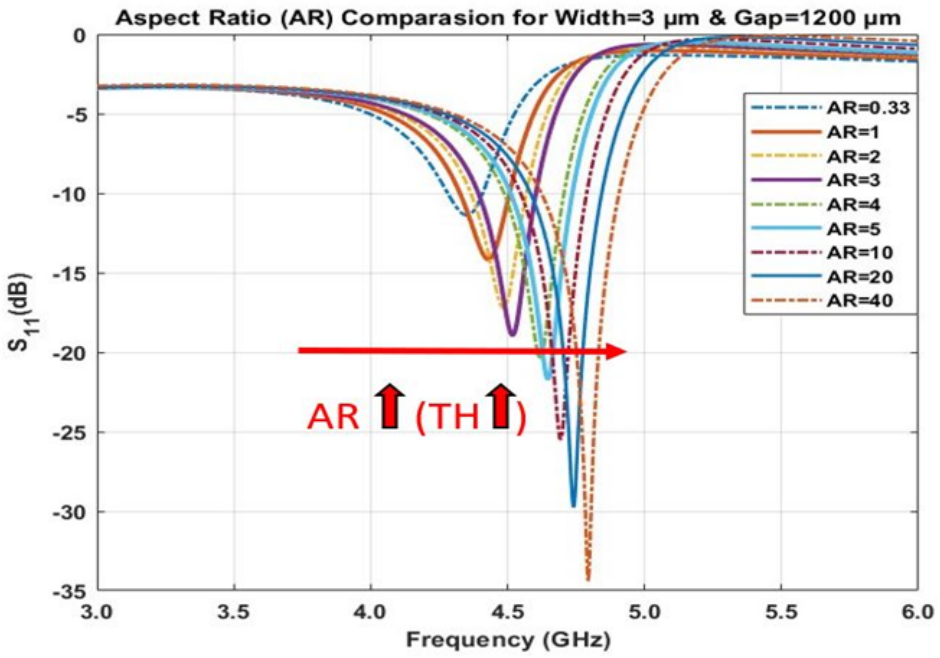

Figure 3.3: Numerical results using simulation setup 1 parametrized with respect to systematically varied cross-sectional aspect ratios (from AR=0.33 to AR=40) by changing the metal thickness from 1 to 120 µm while keeping the width (3 µm) and the gap (1200 µm) fixed.

In Figure 3.4, the importance of the aspect ratio and thus the metal thickness is observed. The variation in the metal thickness shifts the resonance frequency and also changes the Q-factor. Here, with the thicker metal, we find that the Q-factor is improved while the resonance moves to larger frequencies. However, we also observe in Figure 3.4 that this effect diminishes after some large enough aspect ratio (AR $\approx$ 10,20). This is due to predominantly inductive circuit behavior.

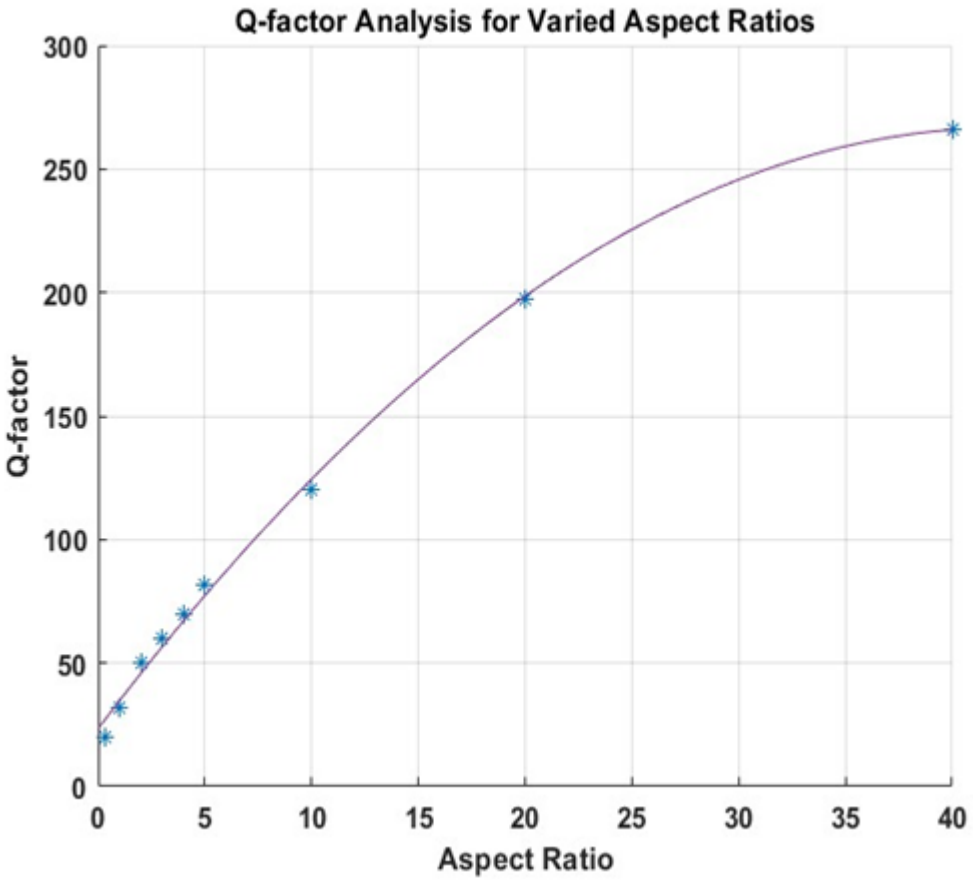

Figure 3.4: Q-factor as a function of aspect ratios numerically computed using simulation setup 1 by changing metal thickness.

Figure 3.5 shows that resonance frequency increases and Q-factor enhances when the cross-sectional aspect ratio increases using the simulation setup 2 similar to the results of simulation setup 1.

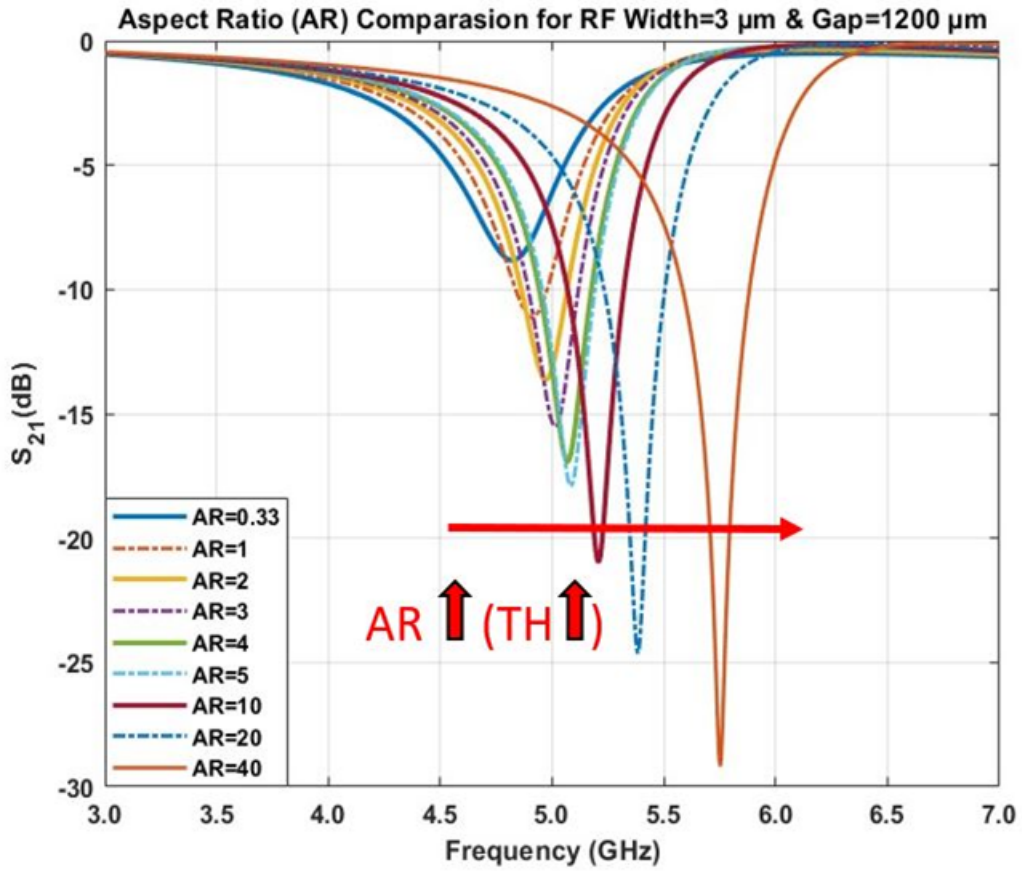

Figure 3.5: Numerical results using simulation setup 2 parametrized with respect to systematically varied cross-sectional aspect ratios (from AR=0.33 to AR=40) by changing the metal thickness from 1 to 120 µm while keeping the width (3 µm) and the gap (1200 µm) fixed.

Figure 3.6 shows that the metal thickness is not very effective to further increase, the aspect ratio after a certain point, for example, after AR $\approx$ 10,20, similar to simulation setup 1. In addition, using numerical simulation, decreasing the gap dimension and increasing the width dimension were simulated to observe the resonance frequency shifts. The reason for these sets of systematic variations is to show that the increasing capacitive behavior is more predominant in the resonance frequency shifts when it is compared to previous results for which the circuit behavior was more predominantly inductive.

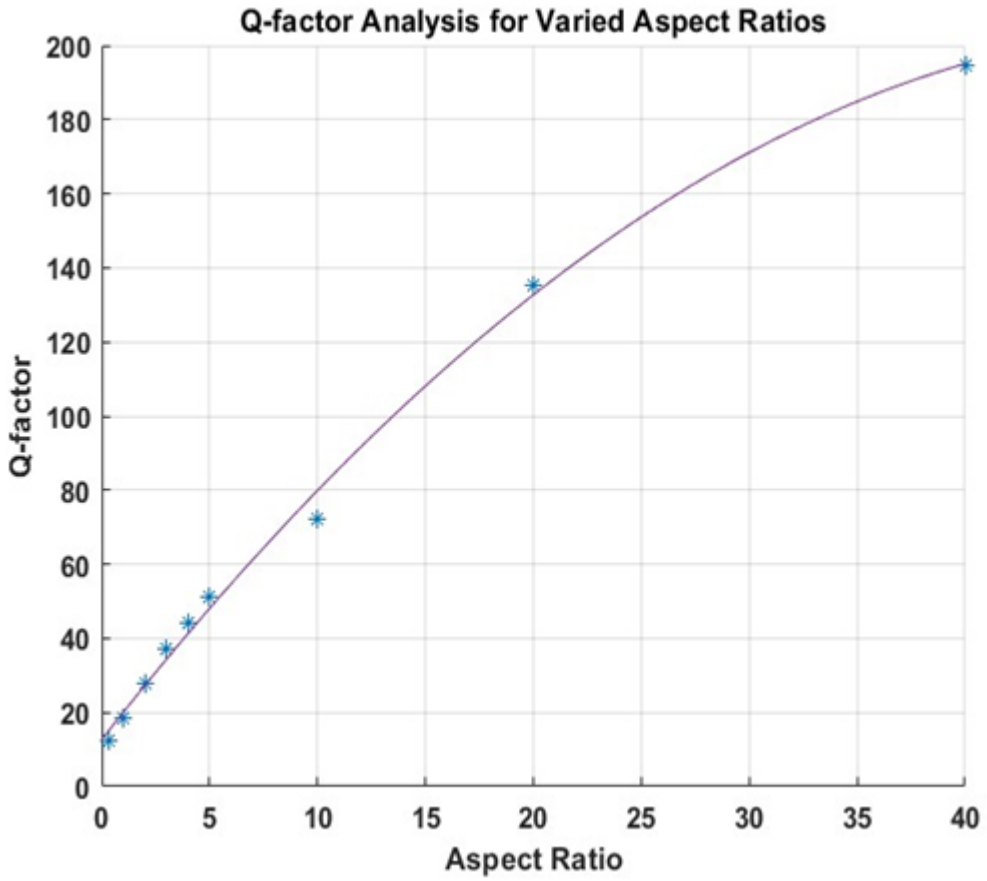

Figure 3.6: Q-factor as a function of aspect ratios numerically computed using simulation setup 2 by changing metal thickness.

Figure 3.7 shows that resonance frequency decreases when the metal thickness increases. Here, with thicker metal, we observe that capacitive behavior increases predominantly, and it leads to decreasing of the resonance frequencies.

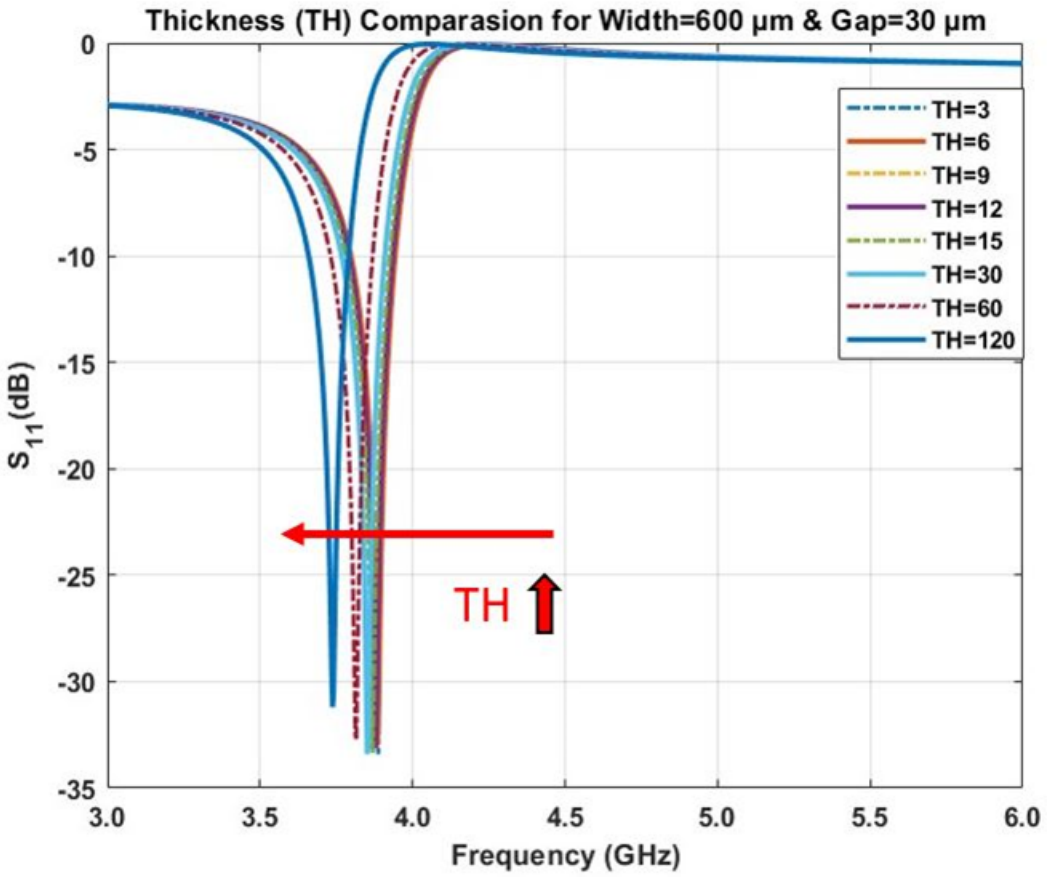

Figure 3.7: Numerical results using simulation setup 1 parametrized with respect to systematically varied metal thickness (from TH=3 µm to TH=120 µm) while keeping the width (600 µm) and the gap (30 µm) fixed.

Figure 3.8 shows that resonance frequency decreases when we increase the metal thickness of the resonator. The capacitive behavior of the resonator increases more, and it results in decreasing of the resonance frequencies similar to the results of simulation setup 1.

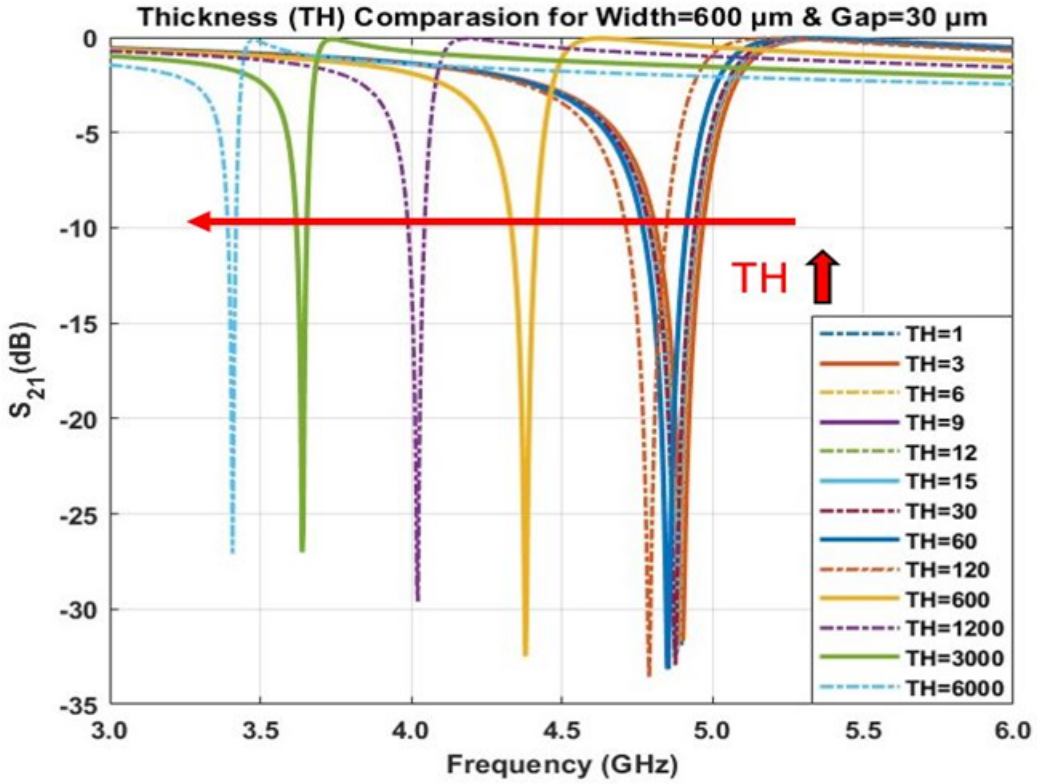

Figure 3.8: Numerical results using simulation setup 2 parametrized with respect to systematically varied metal thickness (from TH=1 µm to TH=6000 µm) while keeping the width (600 µm) and the gap (30 µm) fixed.

In all of these numerical studies, we investigated this deep-trenched class of RF metastructures with a cross-sectional aspect ratio increased to observe strong enough third-dimension effect in comparative analyses of the resonance frequency shifts and Q-factor. We have later used these RF structures to apply our process flow to fabricate them. To this end, we needed an experimental setup to characterize our fabricated RF metastructure resonators. To measure the S-parameters of these resonators, we used a system providing the coupling through our fabricated resonator on the same substrate. We determined to use a microstrip ring

like an antenna for our measurement setup.

3.2 Simulating Microstrip Ring

A microstrip ring was used for experimental measurement of our fabricated RF metastructure ring resonator with the help of near-field coupling. In designing the microstrip ring, an FR4 substrate with 1.6 mm thickness and 4.3 dielectric constant was used. This consists of a ground plane (backside of the PCB), feed lines, and a planar microstrip ring (frontside of the PCB). Figure 3.9 (a) and (b) shows the microstrip ring and its dimensions. Moreover, the SMA connector was designed for driving to obtain more accurate results between the simulation and experiment.

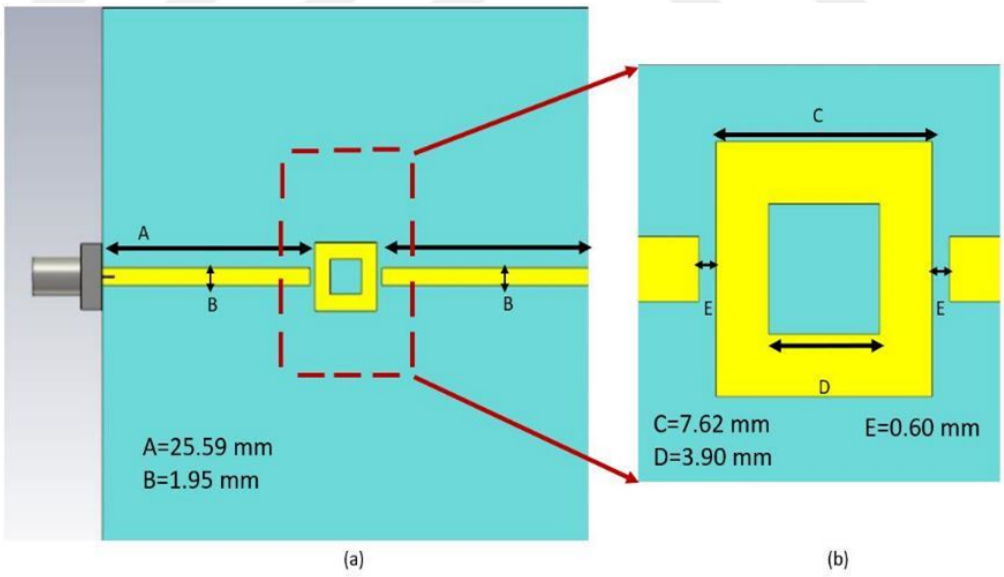

Figure 3.9: Microstrip ring: (a) microstrip ring with the feed line and (b) its zooming along with the dimensions for the microstrip ring geometrical parameters.

The location where our fabricated resonator is to be placed over the microstrip ring is essential for the sensitivity and accuracy of the measurement. Thus, electric field analysis was performed in the simulation tool to find where the electric field was more localized. The fabricated resonator should be located where the electric field (E-field) is the strongest.

Figure 3.10 shows that the electric field is more concentrated in the coupling gap. The distance of the coupling gap was optimized by decreasing the gap dimension to obtain a strong E-field in this region [43]. In Figure 3.11, the microstrip ring's result and the glass substrate's effect are observed when we place it over the coupling gap.

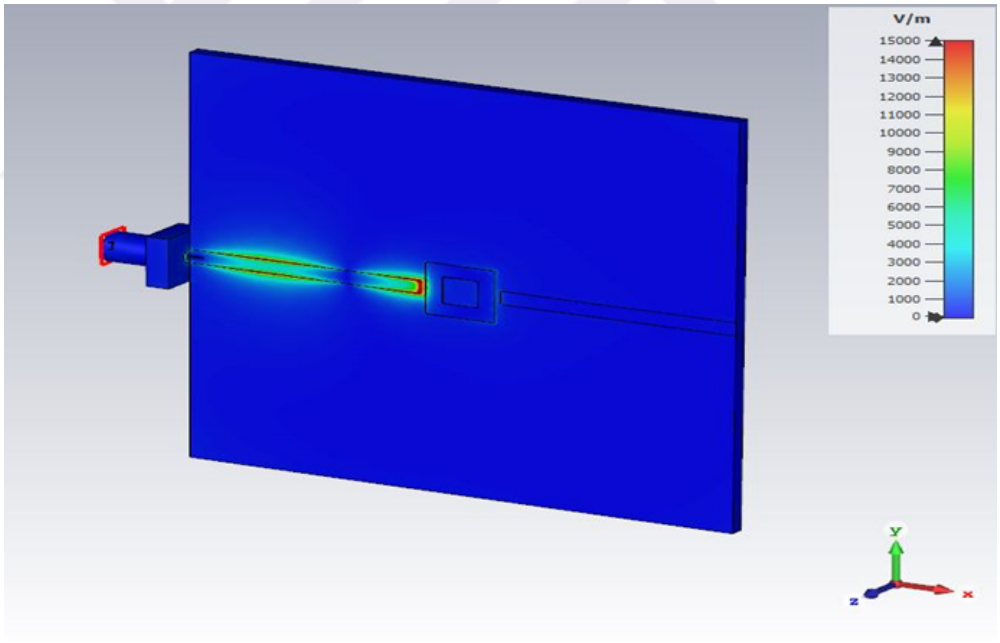

Figure 3.10: Electric field map of the microstrip ring.

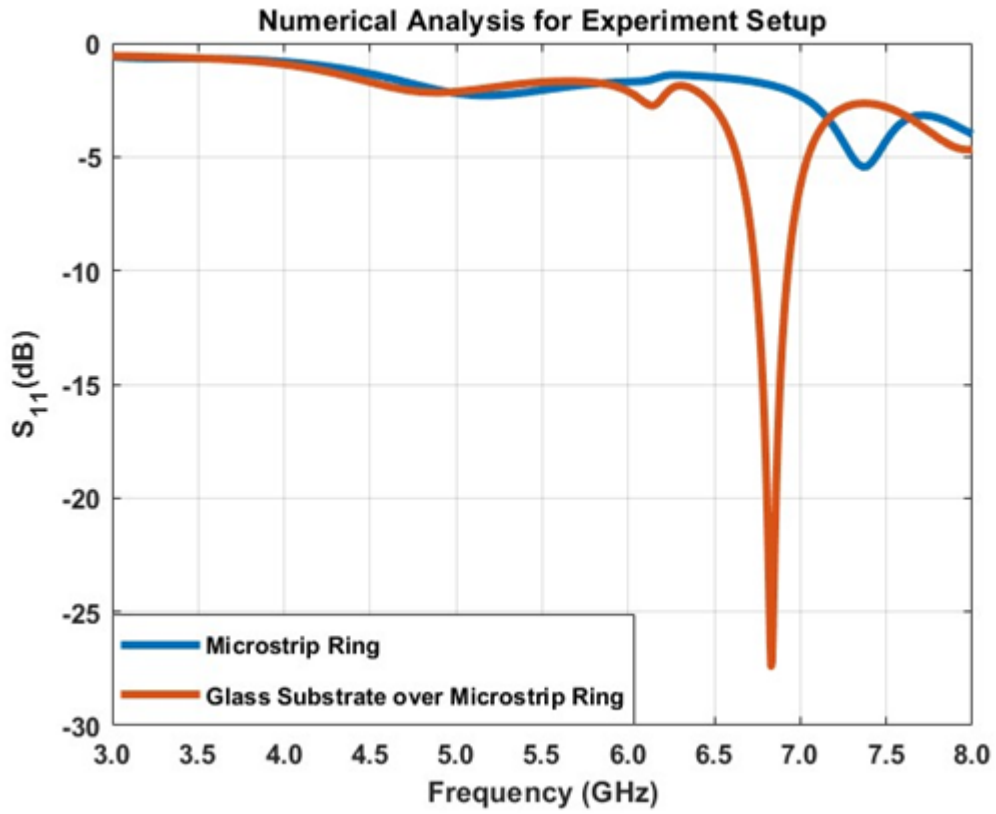

Figure 3.11: Numerical analysis for the microstrip ring and the glass over the microstrip ring.

3.3 Stimulating Experimental Setup

The microstrip ring was employed as a tool helping to take measurements of our fabricated RF metastructure resonators. Thus, these resonators were placed over the coupling gap, and we observed the resonances in S-parameters. Here, the microstrip ring was used as an antenna to detect the resonances experimentally. In Figure 3.12, the experimental setup with the resonator is depicted to be numerically simulated.

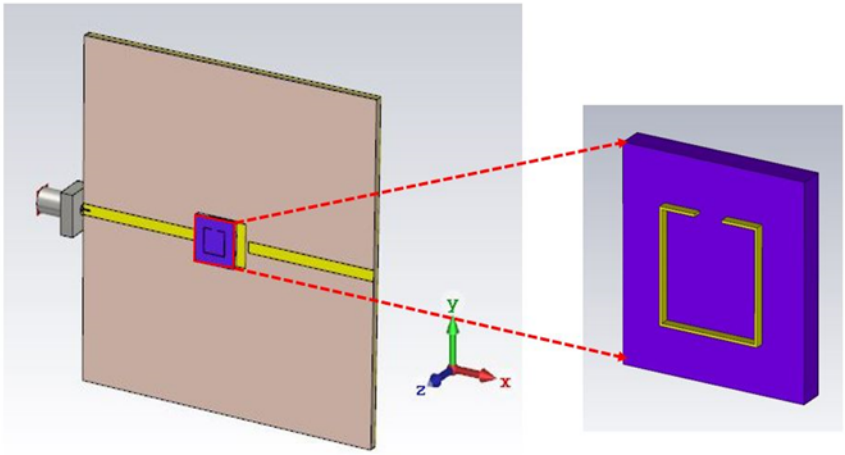

Figure 3.12: Numerical simulation of the experimental setup with our RF metastructure resonator on it.

E-field analysis is shown in Figure 3.13 to comprehend how to find resonance frequency with this experimental setup. When we place the resonator over the coupling gap, there is a strong electric field in the gap.

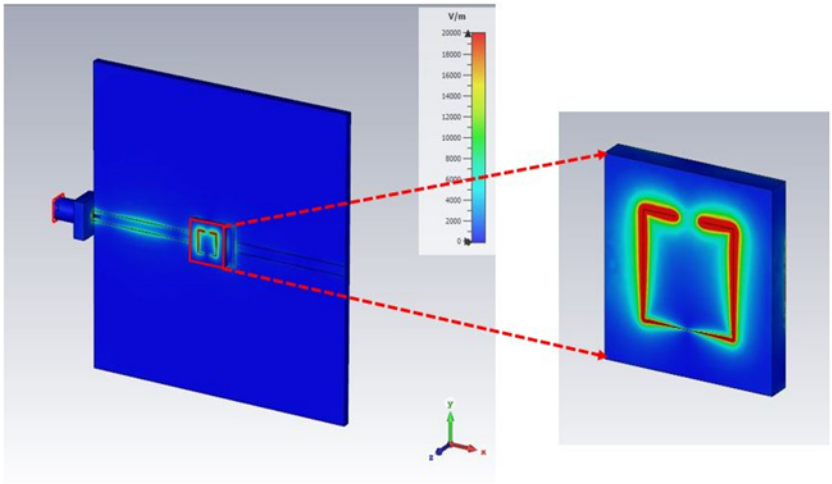

Figure 3.13: Electric field distribution of the experimental setup with our RF metastructure resonator on it.

The resonance frequency due to our RF metastructure resonator is found around 5 GHz in the reflection coefficient. Also, the cross-sectional aspect ratio effects on the resonance frequency and Q-factor using this experimental setup are found in the numerical simulations, observable in Figure 3.14.

Figure 3.14 shows that there is no resonance frequency around 5 GHz when the glass substrate, which does not have a metastructure on it, is placed over the coupling gap of the microstrip ring. However, when the same glass substrate has the metal parts of the RF metastructure, it is clearly observed that the resonance exists at almost the same frequency as in the cases of using the simulation setup 1 and 2. In addition, the behavior of the resonance because of the third dimension effect is similar to our previous numerical results, which show increased resonance frequencies with the increasing aspect ratios while having the split gap (1.2 mm) and metal width (3 µm) fixed.

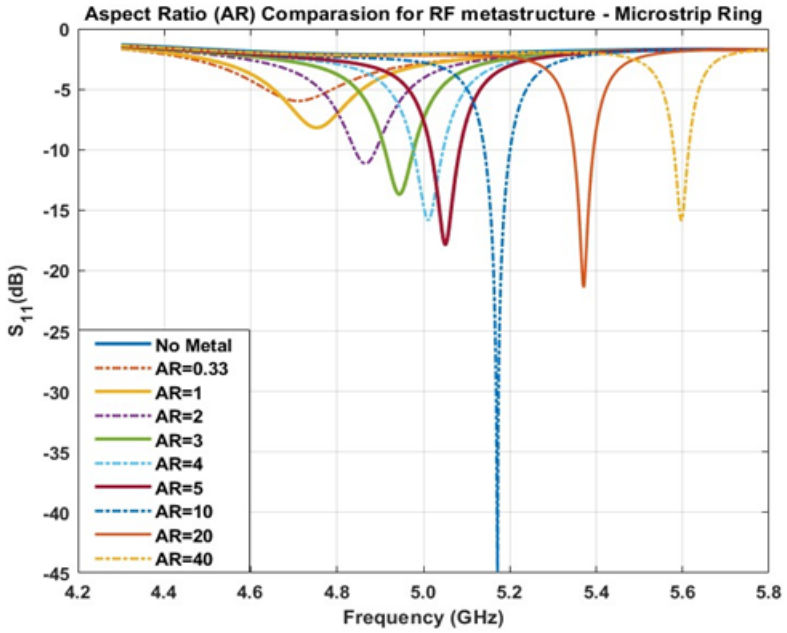

Figure 3.14: Numerical simulation for the aspect ratio effect for our RF metastructure using the microstrip ring.

Following the numerical analyses regarding the effect of dimension variation of RF metastructure, we can move onto our main aim, which is the development

of the proposed fabrication technique along with the recipes of every fabrication step and the entire process flow to construct micro-3D-sculptured deep trenches, electroplating for thick metal deposition and dry etching for the seed layer removal.

Chapter 4

Fabrication of our High Aspect Ratio RF Metastructures

This chapter is based on our manuscript prepared by *Anıl Çağrı Atak, Emre Ünal, and Hilmi Volkan Demir*, which is in submission (2023).

Three-dimensional (3D) printing techniques offer new design capabilities, and we propose and develop a new fabrication process flow based on 3D-printing with 2PP. The proof-of-concept model demonstration is RF metastructures concerning the depth effect as the third dimension. Numerical solutions helped us to design RF metastructures with corresponding dimensions. After analyzing numerical solutions in Chapter 3, we are now at the phase stage of the fabrication process for the simulated RF metastructures by merging the 2PP to construct micro-3D-sculptured deep trenches and other micro-fabrication methods as fundamentally electroplating and dry etching. In this chapter, Section 4.1 explains the 2PP-based 3D printing to construct desired patterns, Section 4.2 discusses the electroplating (on the ITO seed layer) and mechanism to obtain improved electroplated copper, and Section 4.3 presents the etching process of the seed layer. In addition, intermediate steps of the process flow (see all parts of Figure 4.1) including protecting layer implementation, dicing saw procedure, removing the photoresist, and rapid thermal annealing are included within those parts of

this chapter.

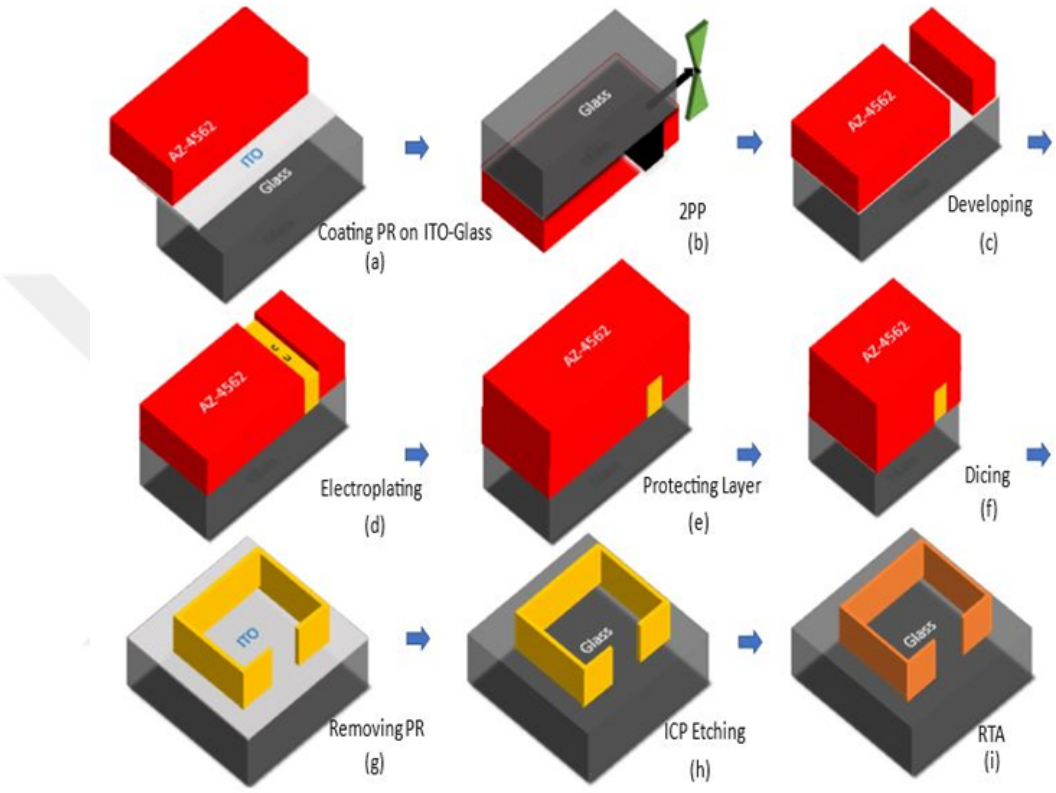

Figure 4.1: Proposed process flow. The developed fabrication methods consist of the following steps: (a) Spin-coated AZ-4562 positive photoresist over ITO-coated glass, (b) placing the prepared substrate on the sample holder of the 3D printing system and exposing light to obtain the desired pattern, (c) developing the exposed part of the photoresist, (d) thick film deposition of copper metal over ITO seed layer along the line of the given pattern, (e) spin-coated the protecting layer, (f) cutting the substrate into smaller pieces with a dicing saw, (g) removing the photoresist, (h) dry etching of the ITO seed layer with ICP, and (i) thermal annealing to strengthen copper structure.

4.1 Two-Photon Polymerization

Based on 3D printing technology, as the main fabrication step of our process flow, we use a 3D printing system (Microlight3D printer is seen in Figure 4.2) based on two-photon polymerization to build our high aspect ratio pattern. Here, we established deep trenches using this two-photon lithography 3D printing system.

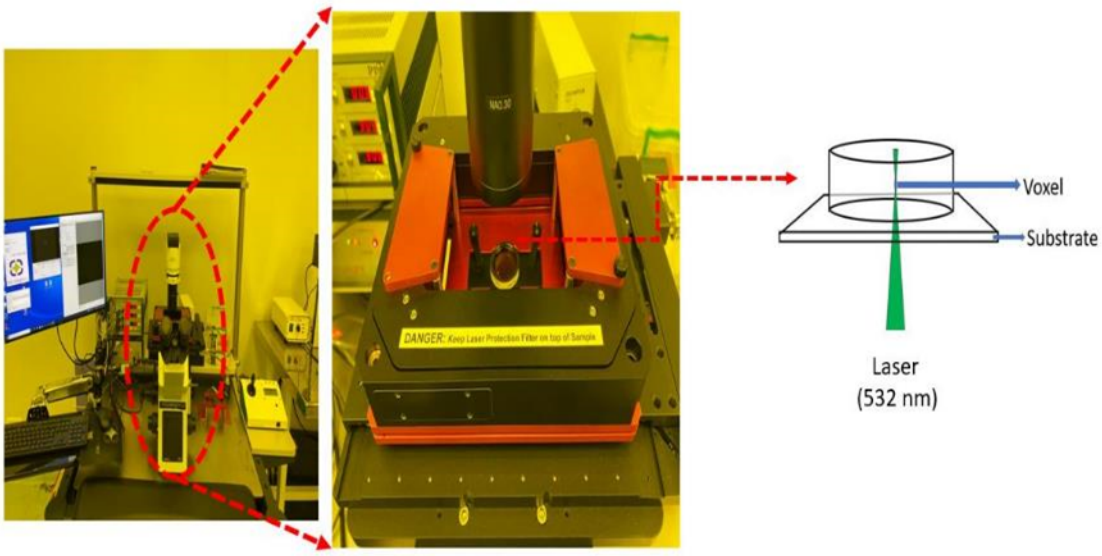

Figure 4.2: The Microlight3D Printer based on 2PP and its general mechanism.

Before moving to the exploration of the 3D printing system, the initial step is to determine the substrate in our process flow. We have considered that there are some requirements in the selection of our substrate. The starting has to be conductive and transparent due to the need for a seed layer in the electroplating process and the effective use in the 2PP process. Thus, we selected indium tin oxide (ITO) coated glass as the substrate. The thickness and the conductivity of the ITO film over the glass were approximately 100 nm and 16 Ω per square, respectively. After cleaning the substrate, we spin-coated positive photoresist AZ-4562 (MicroChem Corp.) on the substrate at 2,000 rpm for 40 s. Then the pre-baking at 110° C oven for 150 s was carried out, and the prepared sample

was ready to put on the sample holder of the Microlight3D. Next, we can move to the 3D printing system.

As mentioned in Section 2.1 two-photon polymerization, the technique is based on the simultaneous nonlinear absorption of two photons to define desired patterns. The system and working mechanism illustrated in Figure 4.2 reveal that the required energy for the chemical activation of the photoresist within the focal cone (except for the focal point) cannot be reached. The required energy, which is proportional to the threshold intensity to start the chemical reaction of photosensitive material, is achieved only in the voxel (small volume near the focal spot) part. Here, the chemical reaction, which is the functionalization of diazotnaphthoquinone (DNQ) and carboxylic acid groups (COOH), starts with the help of the laser at 532 nm wavelength at the focused voxel of this photosensitive material. The chemically activated exposed region becomes more soluble (because it a positive photoresist) and is removed by a developer solution to leave a desired pattern. We can modify the trajectory of the laser beam, which determines the path along which the photosensitive material's chemical reaction to take place. Modifying the path enables us to move the voxel in any direction during the patterning procedure, thereby equipping us with a 3D patterning capability. Furthermore, this adjustment also facilitates the attainment of flat sidewalls of deep trenches, which is an essential requirement for implementing designs with high aspect ratios.

In our demonstration of the proposed process flow, we designed RF metastructure with the help of creating deep trenches. We have implemented RF metastructure resonators in the CST environment, and their patterns were taken from CST as an STL-type file. Subsequently, those files were imported to Simpoly, which is the software of the Microlight3D Printer system to convert files to another file type compatible with the printer system.

To proceed to the 3D fabrication part, we need to compute trajectories by slicing the operation shown in Figure 4.3. The UPLSAPO 20x objective having 0.75 numerical aperture is chosen among 10x, 20x, and 100x objectives for our design specifications. Here, the main part arranges lateral and vertical sizes

through the utilized objective and pattern specifications. The path computations have many options in the advanced parts shown in Figure 4.3.

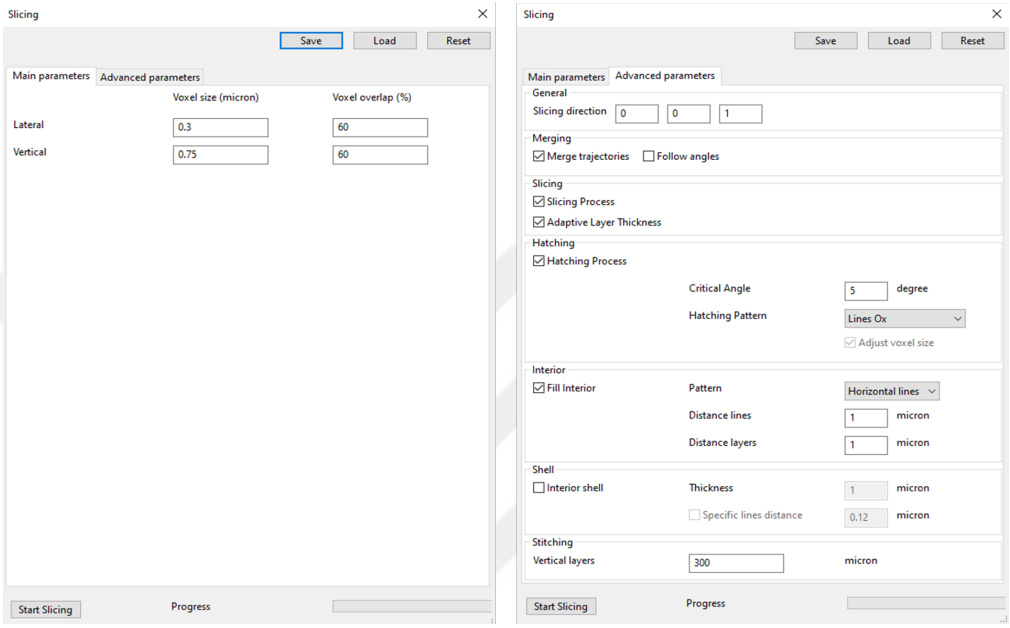

Figure 4.3: Computation of the laser trajectories.

The slicing direction was chosen [0 0 1] because the structures have a deep third-dimension effect in the z-direction, and this direction is more appropriate for our case. The slicing process was applied to define the paths through the structure's walls. Here, an adaptive layer thickness was also selected. It is related to the diminishing of the staircase effect. In our case, there was no possible staircase effect, but a structure having ovality needs this adjustment to save itself from the staircase effect. Thus, the use of adaptive layer thickness is generally preferable. In addition, merging trajectories are generally used to reduce the number of paths, positively contributing to the fabrication speed. The hatching option was also turned on. This is responsible for nearly planar 3D shapes having less than a 5° critical angle and gives extra pathing for both the bottom and top sides of the structure. It decreases the chance of non-exposed parts of the structure at the interfaces, contributing to quickly developing the structure's procedure. When negative photoresist was used, such as OrmoComp and SU-8, there was no need to use the interior filling option to compute laser trajectory. The curing of walls with those slicing options is sufficient to obtain a pattern

since the curing of those provides hardness, and the liquid part remains trapped interior of solid parts. This provides a faster fabrication procedure because of having fewer paths.

On the other hand, in our case, we used AZ-4562 positive photoresist. Therefore, we needed paths to expose the interior part of the structure. Optimizing the filling of interior parts was essential to obtain an entire structure. If the laser trajectory uses too intense beam in general, there might be some voxel parts that burn the photoresist, which later the developer does not remove. In order to prevent the photoresist burning, laser trajectory should be well-defined and optimized according to the structure, the photoresist type and the thickness.

Figure 4.4 shows the laser trajectory for part of our case to understand the mechanism. Red lines, in Figure 4.4 (a) and (c), come from the slicing option, which are located on the walls. The white zigzag parts, in Figure 4.4 (b) come from the filling interior part.

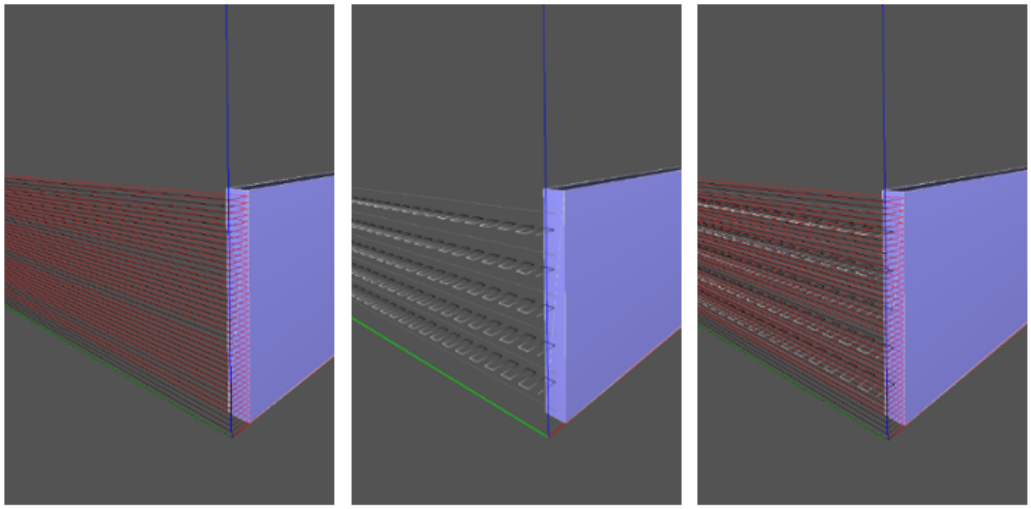

Figure 4.4: Computation of the laser trajectory with (a) slicing, (b) the lines filling the interior, and (c) in combination.

Hatching operation is required for 3D patterns having planar surfaces, illustrated in Figure 4.5. In summary, 1-1.25 µm voxel sizes and 50-60% voxel overlap with slicing having adaptive layer thickness, hatching and filling interior having 1-1.25 µm on both distance lines and distance layers were performed. After finishing the computational part of the trajectory, it should be exported for another software package Lithos. Here, the objective's numerical aperture and the resin's refractive index had to be entered as 0.75 and 1.56, respectively. While the laser gain was constant, path sorting should start from the top since we placed the prepared sample face-down to avoid diffraction from the substrate and generated steeper and deep trenches.

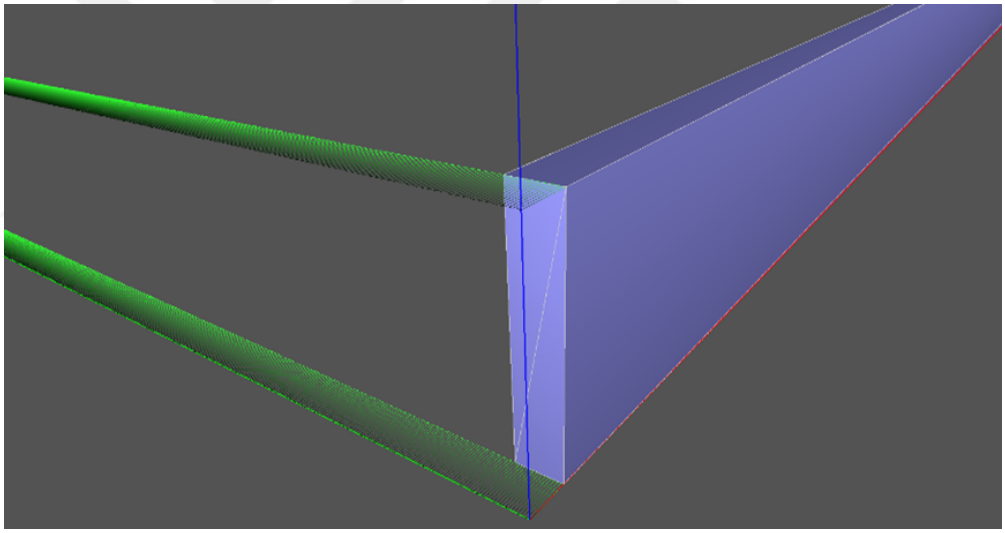

Figure 4.5: Hatching effect on the laser trajectory with green horizontal lines.

Focal point adjustment is crucial to determining the interfaces and designing the procedure through Lithos software. Locating the focal point at the correct interface, which is the interface between the substrate and the photoresist, was required. Otherwise, we could not obtain the pattern properly. During this adjustment procedure, we selected an opaque substrate and correct objective magnification as the fabrication parameters. Although a transparent substrate was utilized in our process flow, the reason for choosing an opaque substrate in the system is due to the flip-down configuration of the sample like an opaque substrate to prevent diffractions from the substrate. We used the camera systems of the

Microlight3D to find the location of the focal point by changing the z-axis. After adjusting the focal point illustrated in Figure 4.6 (a) and (b), the dosage matrix was applied by changing laser gain from 0.200 to 0.020 with the exposure range of 500 µs – 10000 µs. From the dosage matrix, the appropriate laser gain and exposure range were determined to be 0.055 laser gain and 1500 µs exposure time, respectively. We applied them as the design parameters in our implementation.

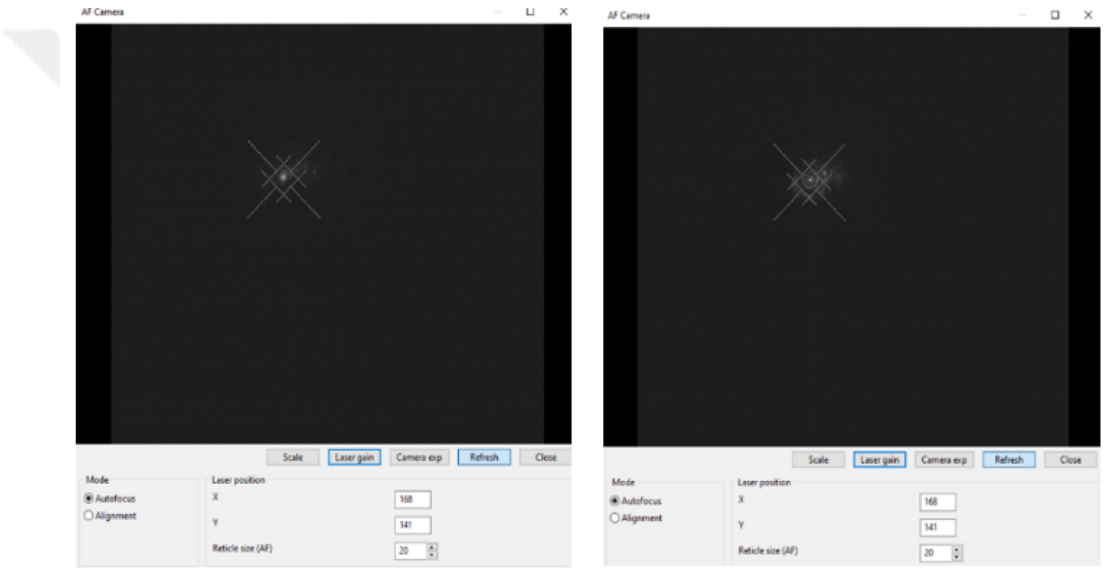

Figure 4.6: Adjusting focal point by changing z-axis. The first focal point (a) shows the interface between air and resin, and the second focal point (b) shows the interface between resin and substrate.

The next step in the process was to develop the photoresist to leave the deep trenches using AZ-400K developer (manufactured by MicroChem Corp.) mixed with deionized water in a 3:1 ratio for 5 min. This solution rate was determined by the rapid development of the exposed region because our structure having a high aspect ratio pattern, as depicted in Figure 4.7 (a) and (b), needs rapid development without ruining the flatness of trenches due to over-developing. At the end of this step, the pattern of the RF metastructure was defined with the help of the 3D printer, ready for the following fabrication steps.

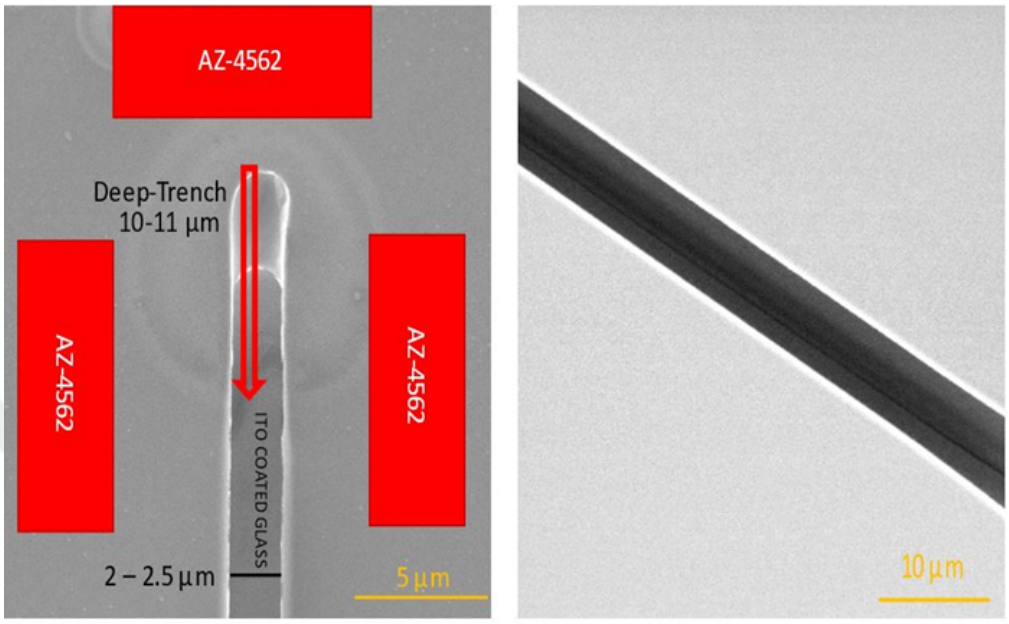

Figure 4.7: High aspect ratio design pattern with (a) 10-11 µm deep third-dimension and 2-3 µm width and (b) flat sidewalls. (Scale bars: 5 and 10 µm, respectively).

4.2 Copper Electroplating

Electroplating plates a metal on a structure. In this process, metal ions in the electroplating solution are transferred from an anode to a cathode, which is coupled to a lower electric potential as illustrated in Figure 4.8. The electroplating setup consists of a power source, a copper anode, a copper cathode sample having the seed layer, wires, a hot plate stirrer, and a copper electroplating solution.

In the plating procedure, customized current and voltage need to be applied by a source (Keithley-2400). The copper anode is connected to the positive terminal of the source, and the cathode touching the seed layer of the substrate is connected to the negative terminal of the source. They are inside the copper bath solution (high-speed bright copper electroplating solution manufactured by Sigma-Aldrich). This copper electroplating solution consists of cupric sulfate and sulfuric acid with a small amount of hydrochloric acid and organic additives. It

is appropriate for patterns having trenches and vias.

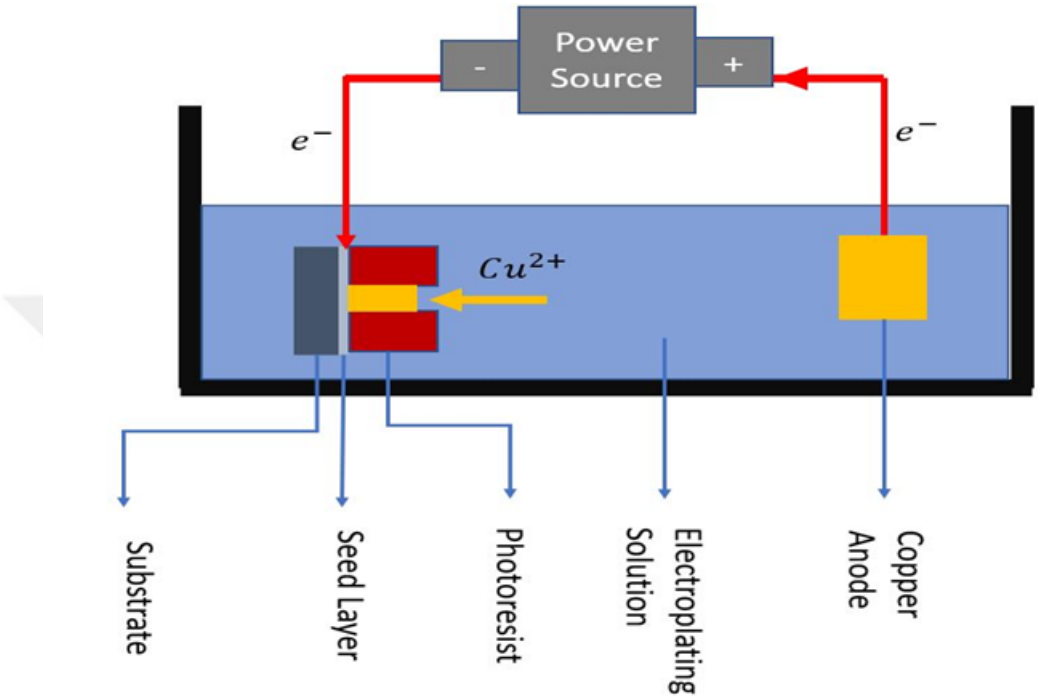

Figure 4.8: Schematic of our electroplating setup.

The prepared device structures, which had already been developed and had a RF metastructure pattern, were ready for the electroplating procedure. There was a need for a conductive surface on the device to conduct a current. Thus, a small portion of the photoresist was removed with acetone from the face of the device. Also, it is worth emphasizing that the cleanliness of the seed layer is critical for depositing metal parts. Before starting electroplating, cleaning with DI water and descumming are generally advised. After cleaning, the cathode connection was supplied with the ITO seed layer shown in Figure 4.9.

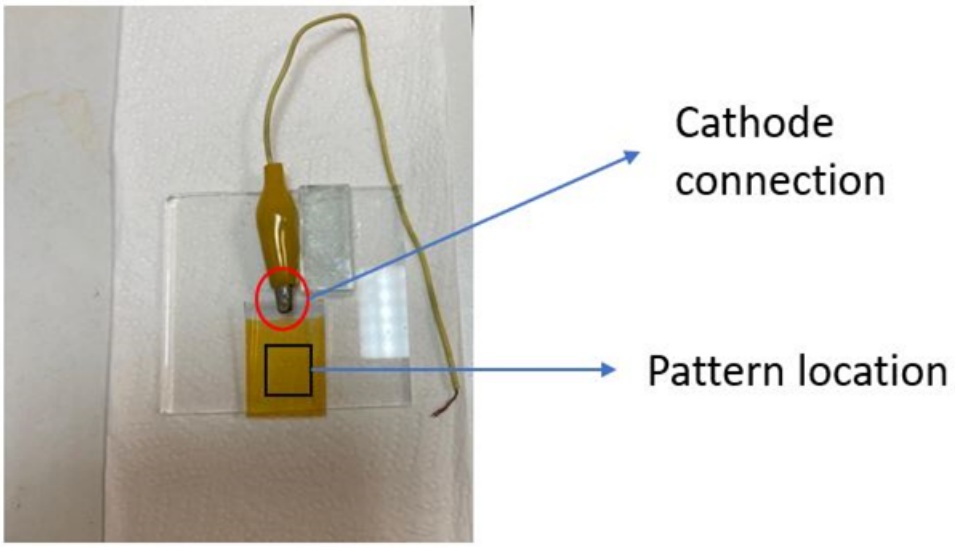

Figure 4.9: A small area of the photoresist removed from the sample to prepare it for electroplating.

The location of the cathode and anode in a beaker is vital for the deposition quality. They must be located vertically and facing each other. It is especially vital for high aspect ratio structures and trenches. Otherwise, some parts of the pattern can have thicker metal parts, and some can have thinner ones, leading to non-uniformity and broken portions. In addition to providing a proper location, we used a hot plate to heat the electroplating solution at 50°C because heating the bath solution provides the required energy for ions/atoms to move around in plating with a stirrer mixing of the copper ions. Using a high stirrer rate during the plating duration results in a non-uniform metal deposition. For this reason, a high stirrer rate was used only before turning on the source, and then it was reduced to 100 rpm. Our electroplating setup is displayed in Figure 4.10.

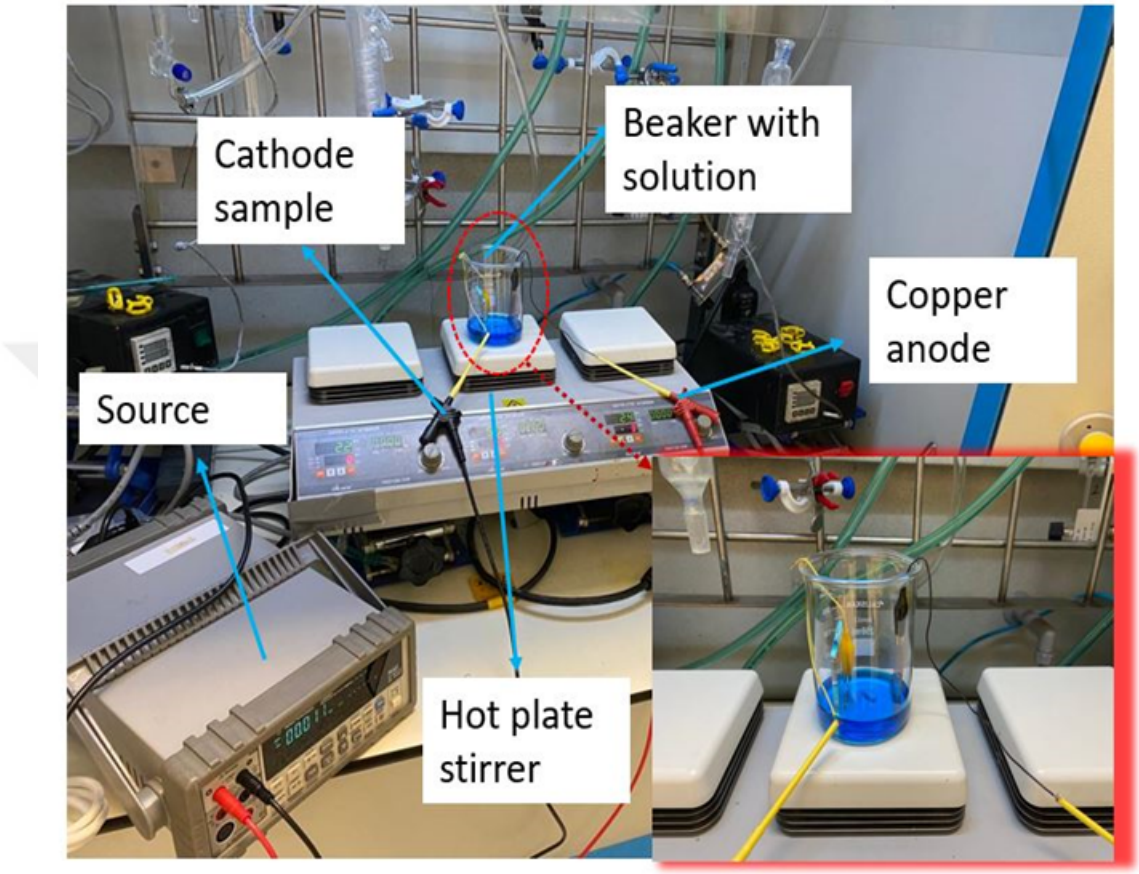

Figure 4.10: Our electroplating setup.

The other critical aspect is related to the source. The possible power sources are voltage and current sources. Here, the current sources are better to use due to their capability to control the height of the metal deposition and allow for a recipe to control time and current relation. Thus, the current sources were first preferred in our electroplating process. It is known that the lower current density provides better results in terms of the deposition uniformity.

In Figure 4.11 (a) and (b), the difference between the high and low current density is shown to understand the importance of the current density. However, problems related to deposition uniformity remain with the lower current density.

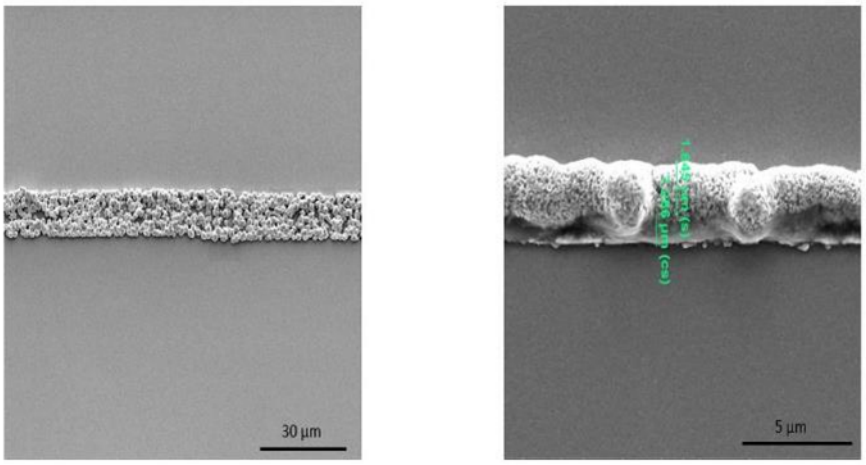

Figure 4.11: Deposition uniformity difference of high current density (a) and low current density (b). (Scale bars: 30 and 5 µm, respectively).

Another method based on customized current signal was employed to remedy these problems. By using lower current density in both forward and reverse directions, it was possible to obtain structures having trenches [44]. A 100 µA forward pulse and a -40 µA reverse pulse were applied to our structure with a 50% duty cycle illustrated in Figure 4.12 (a). This approach yielded better uniformity for the plated parts. However, some local problems still remained in some parts, such as over-plating and under-plating shown in Figure 4.12 (b). These are undesired because there can be some broken parts, damaging the inductive behavior of the RF metastructure.

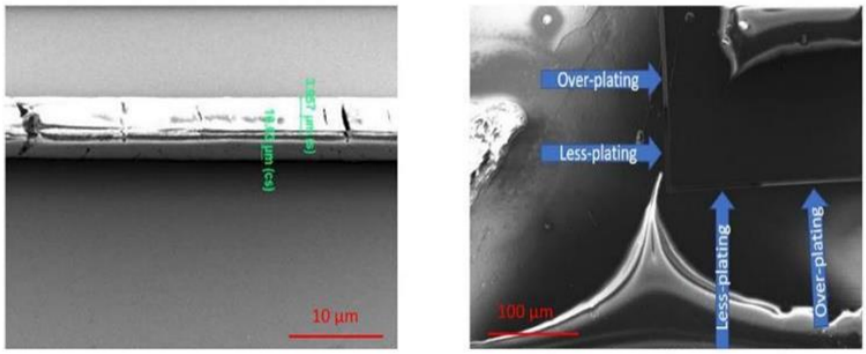

Figure 4.12: Improved uniformity with customized current signal using both forward pulse and reverse pulse for the plated parts (a), over-plating and under-plating problems in some local parts before removing the photoresist (b). (Scale bars: 10 and 100 µm, respectively).

The different diffusion rates of the copper ions/atoms can lead to different plating thicknesses locally in the same structure. Thus, the stirrer was further applied with the customized current pulses.

Figure 4.13 shows that using a stirrer resulted in better mixing of copper ions, and it solved almost all over-plating/under-plating problems, but non-uniformity remained a pending problem.

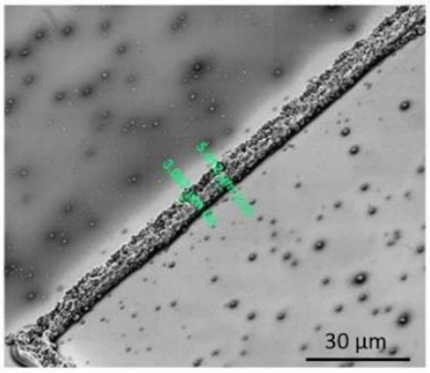

Figure 4.13: Stirrer effect when using along with the customized current source. (Scale bar: 30 µm).

In summary, controlling the height of the plated metal thickness is essential in the electroplating process when using a current source. However, there was a problem related to the uniformity of the plated metal. Using a stirrer mixes copper ions around, and the deposited metal's height was similar in all parts of the structure, but this caused highly non-uniformed electrodeposition. In the light of the know-how, we move to use the voltage source. The controlled voltage provides very uniform deposition. In addition, adding current limitations and using a stirrer at a very low rate along with the voltage source allow for controlling the uniformity of the deposited metal thickness. Figure 4.14 shows that the voltage source yielded better uniformity than the current source.

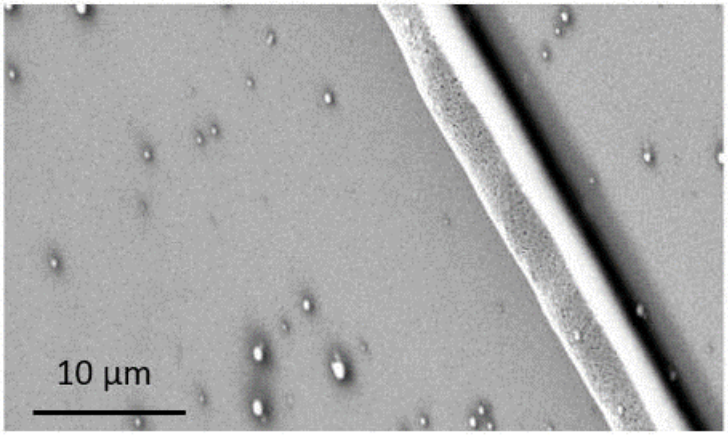

Figure 4.14: Uniform metal deposition when using current controlled voltage source after removing photoresist. (Scale bar: 10 µm).

The recipe of using the voltage source, 100 – 150 mV voltage was applied while having a current limitation of 100 - 105 µA and a heated solution bath at 50°C. Also, we needed to be sure about the cleanliness of the seed layer and vertically placed anode/cathode parts. The stirrer was used before turning on the source with a high rate to mix ions well. Then, it was stopped, or it was decreased to 100 rpm. This recipe had a 750 - 1000 nm-per-min deposition rate in our case. After thick metal film deposition, we cut the substrate into 8 mm x 8 mm pieces to take experimentally accurate measurements by using a dicing saw. Since the samples had high aspect ratio metal parts, AZ-4562 photoresist (as a protection layer) was coated to protect the resonator's metal parts from damaging during

the dicing operation. After completing the dicing operation, the photoresist had to be removed from our samples to make them ready for the seed layer etching. The photoresist was removed with the help of acetone. Then, we put each one-piece sample inside a beaker containing isopropanol softly. Because a high aspect ratio structure is very sensitive, each piece should be placed gently. The samples we took from the beaker had to be left to dry slowly under the petri dish, or a critical point dryer had to be applied.

4.3 Seed Layer Etching

As mentioned in Section 4.1, our substrate was chosen as a 100 nm thick ITO coated glass. ITO has broad applications in producing optoelectronic and microelectronic devices owing to its good electrical conductivity and high optical transparency. We need to use the conductive seed layer for electroplating purposes. Although other possible seed layers, such as gold, chromium, and aluminum, have better conductivity, they do not have the optical transparency which is needed for two-photon lithography in our case. When a variety of candidate etching types of the ITO were analyzed, wet chemical etching with hydrochloric acid was found to be used most commonly. However, wet etching has several disadvantages regarding reproducibility, directionality, and the risks related to the use of dangerous acids/solvents. Since our structures have high aspect ratio walls, the preferred mechanism had to have process control, repeatability, and vertical etch profiles with sufficient anisotropy [45]. Therefore, inductively coupled plasma (ICP) reactive ion etching system was chosen as the tool for our dry etching methods. This system consists of an RF coil with a 13.56 MHz power supply and two RF platen powers connected to the coil and the electrode. Different available gases such as SF_6, C_4F_8, CHF_3, CF_4, Ar, and O_2 can flow in plasma generated by the RF generator. The system is characterized by low operating pressure; so, it has one mechanical pump and one turbo pump to bring pressure down to the 10^{-6} Torr level. Through the plasma etching process, we effectively have chemical etching, physical etching, or a combination of both chemical and physical etching, as illustrated in Figure 4.15.

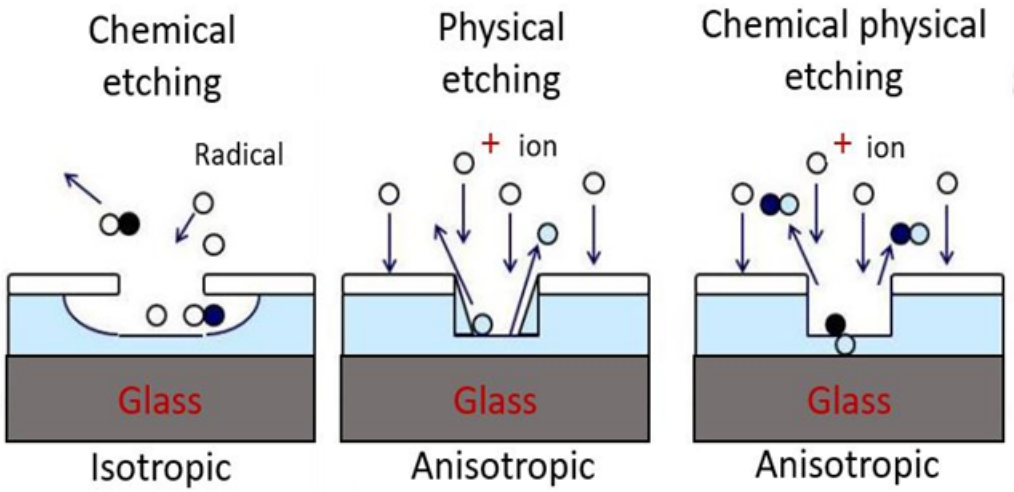

Figure 4.15: Etching processes.

Chemical etching is an isotropic process that results from interactions with radicals, which are reactive chemical species due to incomplete bonding structure. It is similar to wet etching because it has a high etching rate and selectivity. In our case, we have determined CF_4/Ar gas mix because it is known that CF_4 can react with ITO when the right power and pressure conditions are provided in the chamber. This reaction is a chemical reaction between the ITO and CF_4 species. On the other hand, the process of physical etching subjects a material to ion bombardment, which provides anisotropic etching while the etching rate and selectivity are poor [45]. As illustrated in the physical etching of Figure 4.15, sputtered particles can have various emission angles, leading to broken vertical walls. However, it is feasible to regulate the combination of chemical and physical etching mechanisms to have control over the shape. In addition to the chemical reaction between the ITO and CF_4 species in our case, the effects of Ar-ion bombardment play an important role in the physical etching. Mixing chemical and physical etching provides a middle-range etching ratio and selectivity. When our etching purpose is considered as etching ITO parts on non-copper parts of the surface, the process with CF_4/Ar gas mix is sufficient. The primary mechanism is sketched in Figure 4.16.

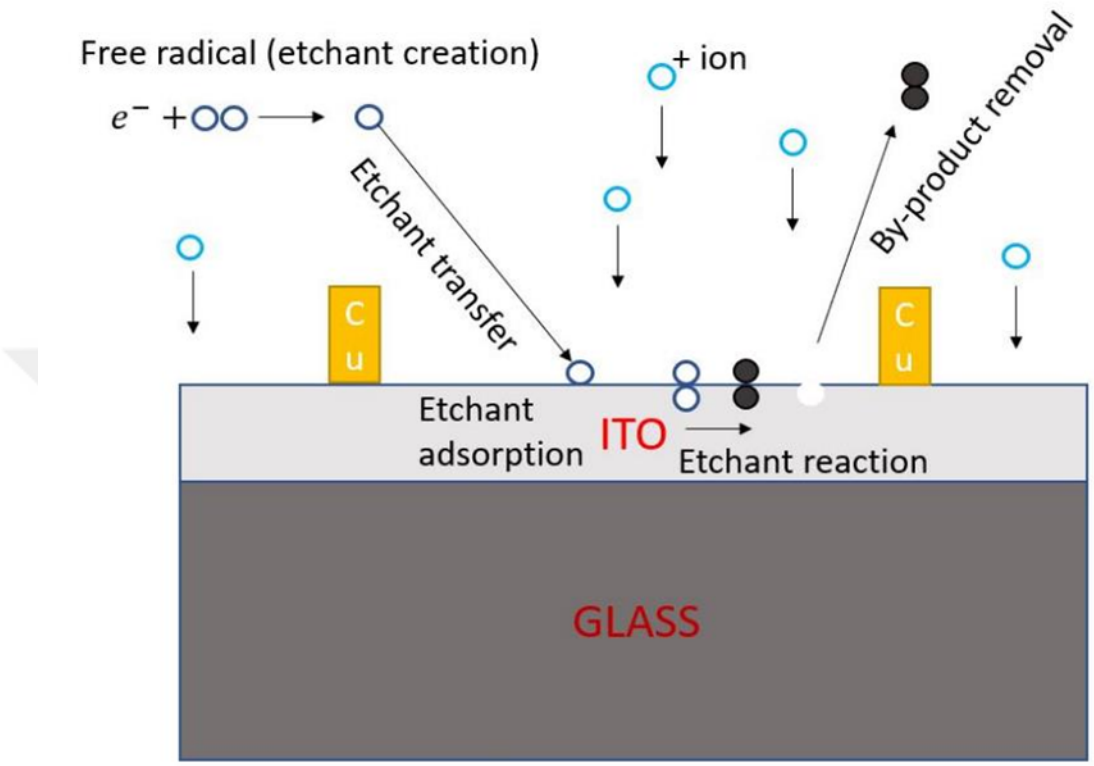

Figure 4.16: Seed layer etching mechanism for our RF metastructure resonator.

In the etching mechanism, we used 20 sccm total gas flow rate, consisting of 18 sccm Ar and 2 sccm CF_4, while the substrate temperature was adjusted to 40°C and the system pressure was 20 mTor. Here, applying RF power increases the etch rate by dissociating more actively CF_4 and increasing the plasma density, and DC-bias accelerates ion bombardment and make more ions reach the ITO surface [46]. According to our ICP system's specifications, approximately 100 nm ITO layer was removed with 500 W RF power and 300 V DC-bias voltage. After being sure of the etching of the ITO surface, we applied rapid thermal annealing to the sample at 500°C for 10 min, which helped strengthen the bonds of copper and enhanced the conductivity of our high aspect ratio metastructures.

Chapter 5

Proof-of-Concept Demonstration of our High Aspect RF Metastructures

This chapter is based on our manuscript prepared by *Anıl Çağrı Atak, Emre Ünal, and Hilmi Volkan Demir*, which is in submission (2023).

In this thesis, a new class of high aspect ratio RF metastructures, showcasing the depth effect as the third dimension, was fabricated as a proof-of-concept demonstration by using the proposed fabrication process flow. Here, we have tested and analyzed these fabricated deep-trenched RF metastructure resonators using our experiment measurement setup. In this chapter, Section 5.1 presents the experimental measurement setup to be used to characterize the fabricated RF metastructure and Section 5.2 describes the structural details of the fabricated RF metastructures. Measurements with the network analyzer to characterize resonance frequency, Q-factor and miniaturization are explained in Section 5.3.

5.1 Our Experimental Measurement Setup

The microstrip ring measurement setup, as illustrated in Figure 5.1 (a) and (b), was fabricated using a PCB milling and prototyping machine (LPKF ProtoMat) based on the geometrical dimensions of its design presented in Figure 3.9. This was used to take measurements from our proof-of-concept model RF metastructure resonators.

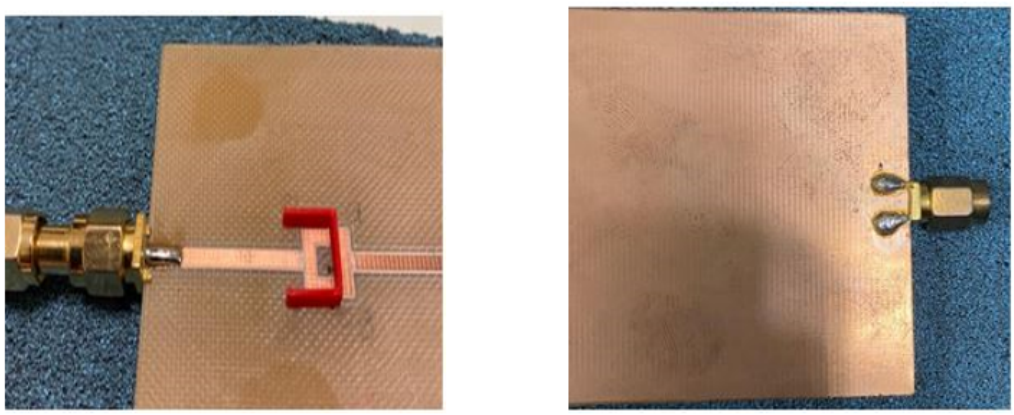

Figure 5.1: Our home-built microstrip ring setup: (a) frontside of the microstrip ring and (b) backside of the microstrip ring.

Changing location of the device over the microstrip ring expectedly shifts the recorded spectrum. Here, the red PLA pattern, not affecting the resonance frequency, marks the coupling region for the resonators to be placed. The location was set to obtain experimental results in agreement with the numerical ones. When we placed the glass substrate over the determined coupling region, the resonance was observed near 7 GHz, and there was no resonance in the frequency range of 4 – 5 GHz.

Moreover, there is another essential aspect. We have tested the substrates made of the glass and the ITO-coated glass in the same ranges of thickness and permittivity. The ITO-coated glass exhibits a resonance frequency near 6.5-7 GHz in our measurements. We have repeated measurements for the substrate independently of other parts of 2PP and electroplating to understand whether the seed layer etching with ICP worked well. We found that the glass substrate and completely etched ITO-coated glass substrate have matched and exhibited the same similarly result as Figure 5.2.

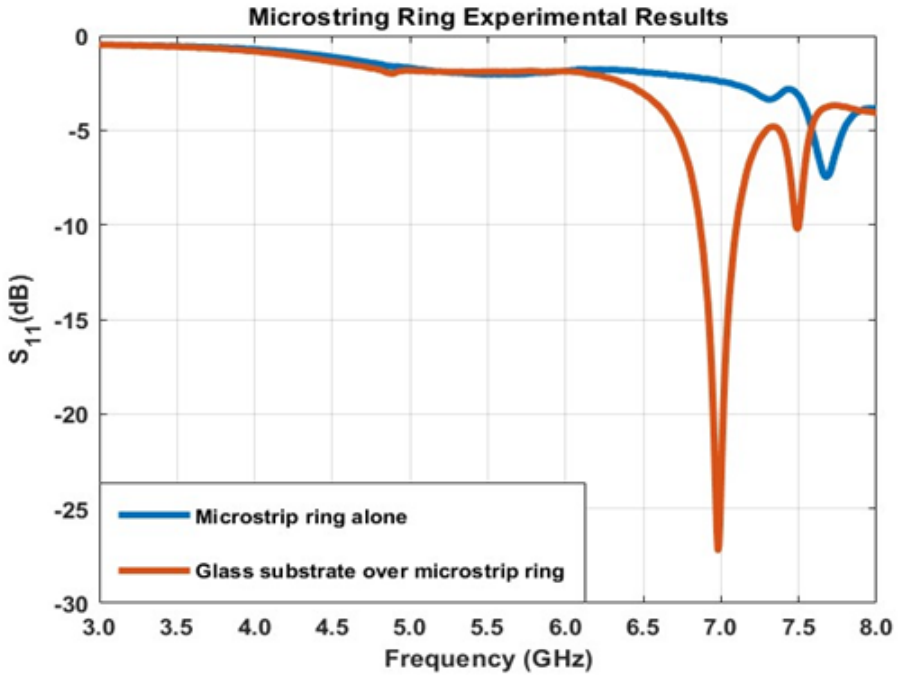

Figure 5.2: S_{11} of the microstrip ring with and without a glass substrate.

5.2 Imagining our Fabricated RF Metastructure Resonators

We have determined the geometrical parameters, illustrated in Figure 5.3 (c), of our RF metastructures with the help of numerical full electromagnetic solutions. Then, we followed the developed process flow to construct our deep-trenched RF metastructures, allowing for a comparative analysis with conventional RF metamaterial resonators fabricated through standard fabrication techniques. In Figure 5.3 (a) and (b), we show that our fabricated resonators feature a much greater total metal thickness and a larger cross-sectional aspect ratio; leading to a larger Q-factor and a smaller footprint working for the similar resonance frequency.

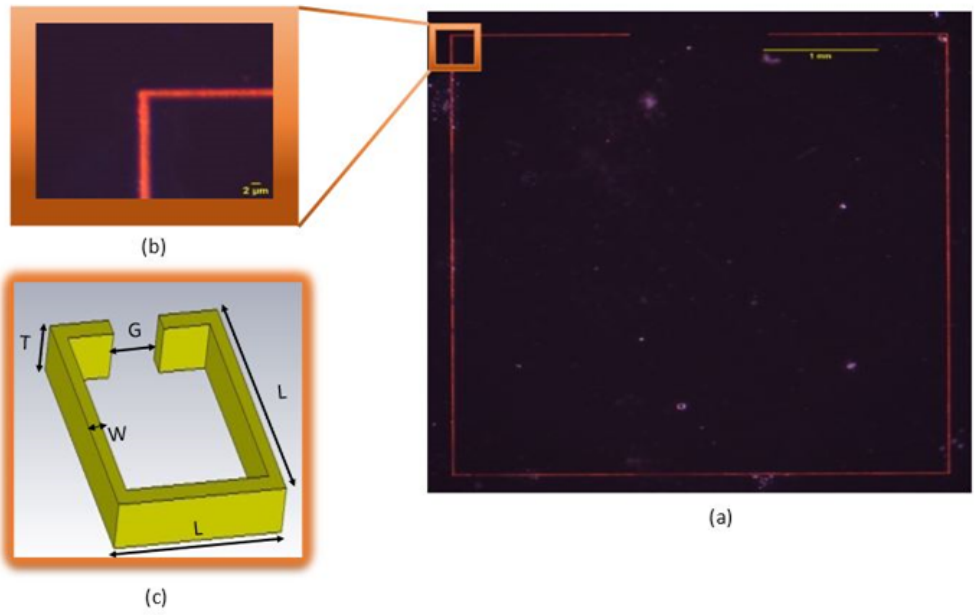

Figure 5.3: Our fabricated RF metastructure resonator using the proposed process flow: (a) Red lines show the metal parts, while dark parts show the glass, (b) zoomed at the corner and (c) with the physical dimensions of the metastructure which are T:4-6 µm, W:2-3 µm, L:4.3 mm, G:1.2 mm. (Scale bars: 2 µm and 1 mm, respectively).

The length of one side of the resonator (the longest dimension) and the metal width (the shortest dimension) are approximately 4.3 mm µm and 0.002 mm, respectively, indicating an enormous ratio of 2,150, as displayed in Figure 5.3. Moreover, the scanning electron microscope (SEM) images of fabricated structures in Figure 5.4 show that the structures have nicely flat metal sidewalls and high aspect ratios of around 1, 2, and 4, respectively.

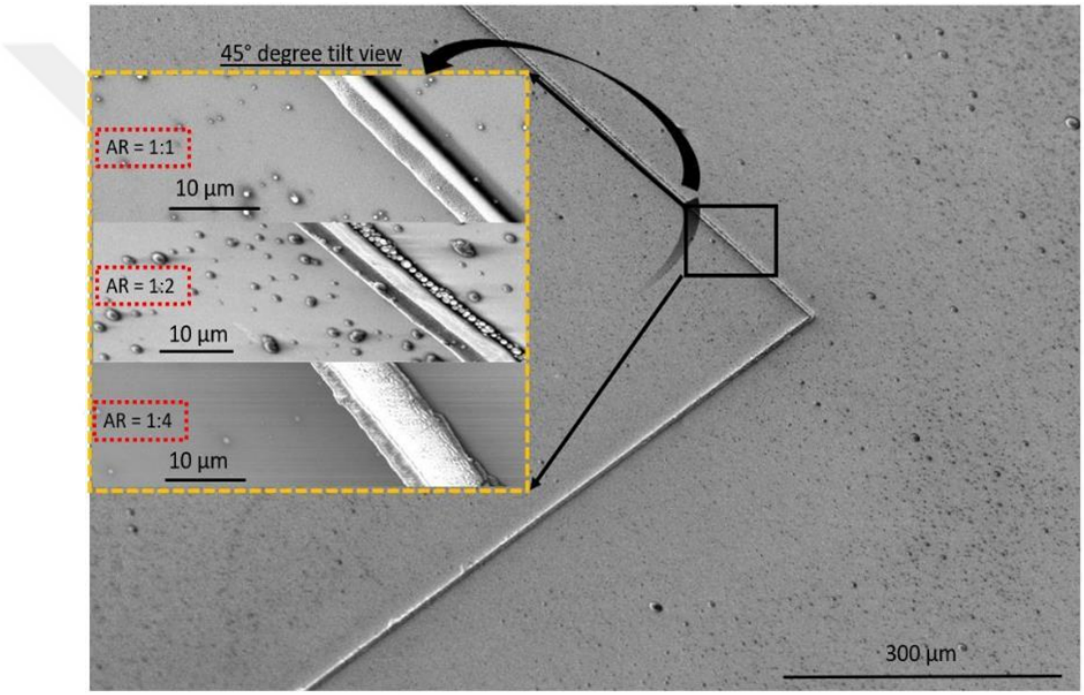

Figure 5.4: Scanning electron microscopy images of our fabricated RF metastructures, shown with the aspect ratios of the metal parts, which are 1, 2, and 4, respectively. (Scale bars: 10 µm and 300 µm, respectively).

The third dimension with deep trenches is emphasized during the discussion of fabrication flow. In the 2PP step, optimizations of computation of the laser trajectory, laser power, and exposure time were critical. Otherwise, over-exposure can cause the burning of the photoresist, or under-exposure cause longer developing times, which is the reason for the deterioration of the structures' sidewalls. Here, adjustments to the electroplating process, which is heating and stirring the solution, also enhanced the quality and the uniformity in the deposition process.

However, it is vital that heating the solution increases the electroplating deposition rate, which means heating can lead to thicker coating for a fixed duration. Thus, the optimization of electroplating duration has to be considered given the temperature of the solution. Also, high stirring rates can damage structures with the mixing force of the liquid since our structures' aspect ratios are high and fragile.

5.3 Testing and Analyzing our RF Metastructure Resonators

Our fabrication approach offers the opportunity to build RF metastructures that allow to tune resonance frequency, raise the Q-factor and reduce the footprint. Metastructure resonators in the resonance frequency range of 4–6 GHz were simulated in CST Microwave Studio to show the importance of the aspect ratio with a comparative analysis of their resonance frequency shift, Q-factor and footprint as a function of the aspect ratios (metal thickness and width ratio). Then, the designed RF metastructures having distinct aspect ratios were fabricated. The results of numerical simulation and experimental measurements are presented.

5.3.1 Resonance Frequency and Q-factor

The Q-factor can be calculated as the resonance frequency divided by the 3 dB-bandwidth [42]. When the metal thickness of a resonator increases while its metal width is kept constant, its Q-factor improves. Our results show that the Q-factor of a resonator with an approximately aspect ratio of 2 is 6 – 7 times larger than that of the resonator with an approximately aspect ratio of 0.25. Also, we examined a larger resonance frequency shift of 200 MHz varying aspect ratios of RF metastructure resonators in both numerical simulations and experimental measurements thanks to the third-dimension effect, as expected. The resonance frequency rises as the metal thickness of the resonator grows because the product

of inductance and capacitance decreases. According to the analytical method for inductance calculation [38], as metal thickness grows, the inductive effect diminishes. The capacitive impact grows according to the capacitance calculation [40]. Because the rate of decline in inductor value is larger than the rate of rise in capacitance, the resonance frequency increases with increasing metal thickness. So, considering the third-dimension effect from the deep trenches, the resonance frequency of the designs can be fine-tuned. Here, the various aspect ratios play an important role on the frequency shifting and improved Q-factor of the resonators as illustrated in Figure 5.5 (a) and (b).

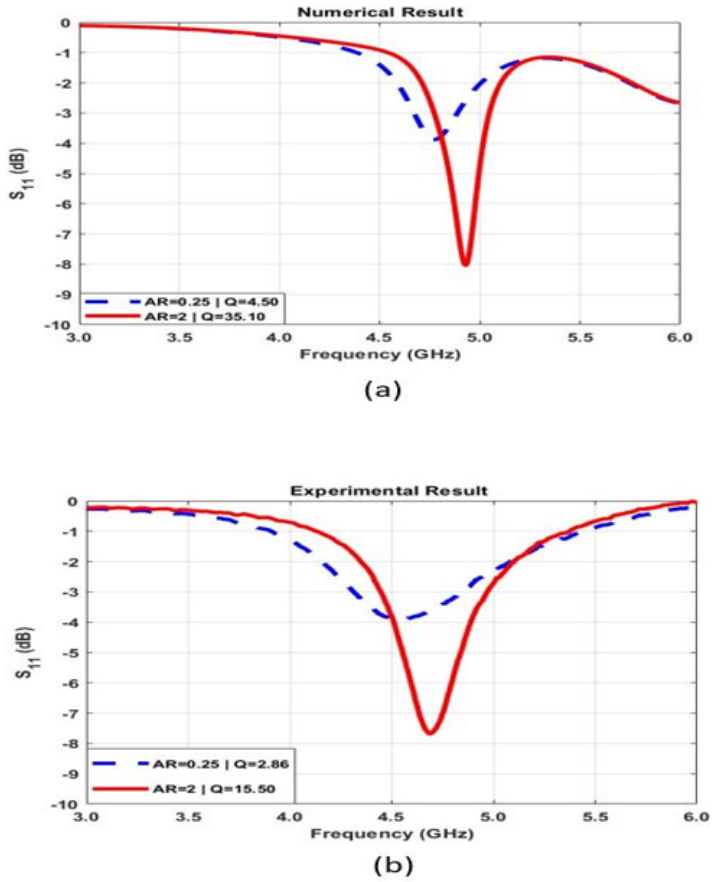

Figure 5.5: S_{11} spectra: (a) Numerical simulation results and (b) experimental measurement result. The resonance frequency and Q-factor increase with the increasing metal thickness while keeping metal width fixed.

Figure 5.6 shows that when the metal thickness increases, the total capacitance increases in both scenarios of the varied width and split dimension. However, it is seen that when the split becomes smaller and the metal width becomes more extensive, the increment of the total capacitance, as a result of the increasing metal thickness, is more considerable. In other words, this capacitance behavior is related to fundamental capacitance formula. In this formula, the capacitance increases when the area of the plates is raised, or the distance of the plates is decreased. In the light of this knowledge, when the split of the resonator is small enough and the width of the resonator is large enough, the effect of the metal thickness, contributing to the area of the plates in the capacitance formula, is more essential to change capacitance value through the increasing metal thickness.

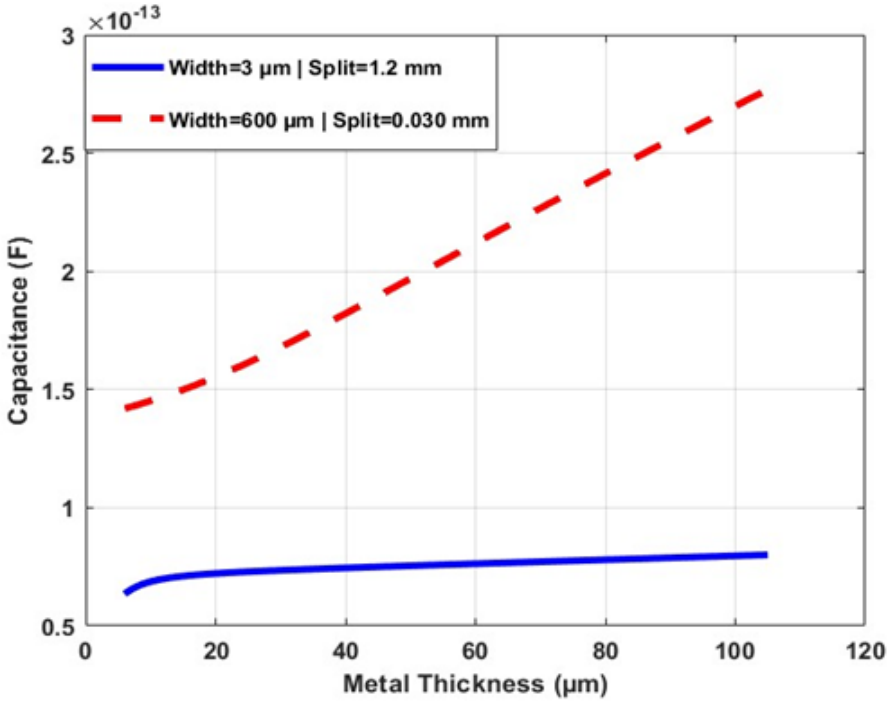

Figure 5.6: Numerical analyses for the capacitance as a function of the metal thickness.

We have analyzed the capacitance change through analytical approaches. Here, Figure 5.7 shows the inductance changes using varied metal thickness in both scenarios which are smaller width and larger split of the resonator, and larger width and smaller split. According to numerical results, the inductive behavior decreases when metal thickness increases in both cases. However, the ratio of the decreasing is more dominant in the smaller width and larger split case.

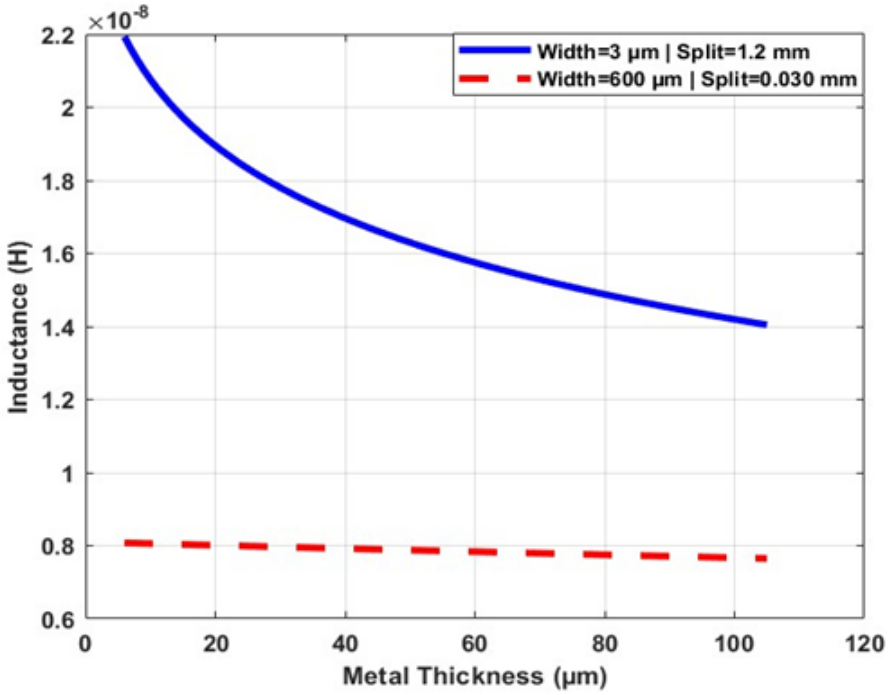

Figure 5.7: Numerical analyses for inductance as a function of the metal thickness.

Observing the numerical results of the capacitance and inductance gives intuition for the resonance frequency change as a function of metal thickness. We found that increasing metal thickness (relatively increasing aspect ratio) is able to change resonance frequency in both ways illustrated in Figure 5.8. Here, the shift direction of the resonance frequency is based on the geometrical dimensions of the geometry due to the change of cases in which the inductive effect or capacitive effect is dominant. Also, our cases, related to our RF metastructure measurements, match the idea of the analytical approach of the resonance frequency.

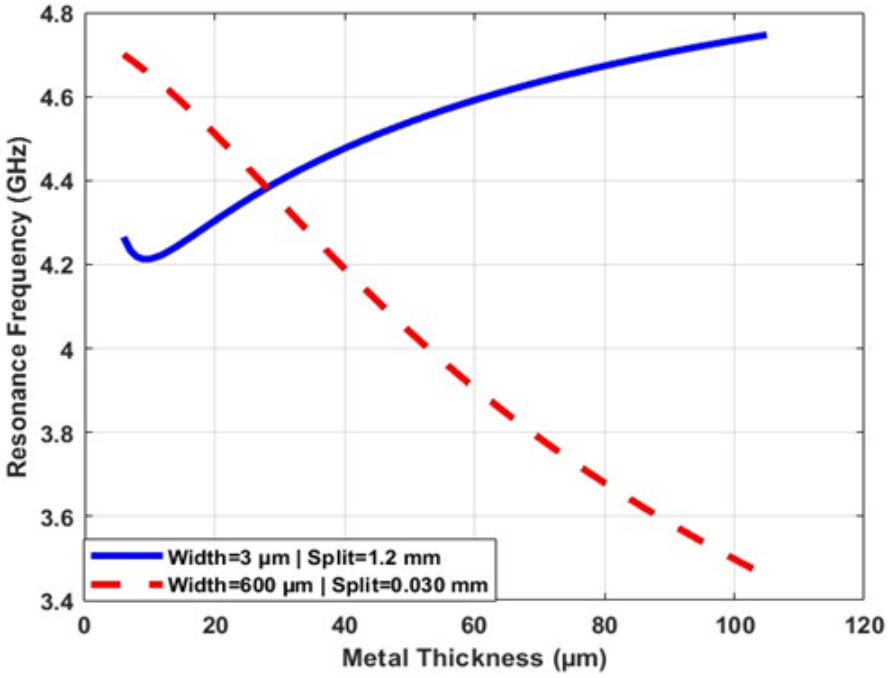

Figure 5.8: Numerical analyses for resonance frequency as a function of the metal thickness.

As a result, we have tested our fabrication approach when we built our RF metastructures, having different aspect ratios. After testing our process flow, we analyzed our results in terms of resonance frequency and Q-factor. It was found that metal thickness, generally ignored in RF structures, extremely have importance for the resonance frequency shit and improved Q-factor. Although numerical simulations and experimental measurement matches, we give place the analytical approaches to support our results of RF metastructure. Here, numerical analyses, using the LC equivalent circuit of the RF metastructures, also supports the idea of effectiveness of the deep trenches used in RF metastructures.

5.3.2 Miniaturization

Figure 5.9 and Figure 5.10 show two different resonators with the exact substrate sizes: an SRR RF metamaterial produced using conventional LPKF PCB machine techniques and an RF metastructure created using our proposed methodology. The width of the RF metastructure was determined to be sub-10 µm with a 1.2 mm split dimension and 4.3 mm one-side length. However, the LPKF machine had a constraint on the metal width, with a minimum width of 0.6 mm. Therefore, the resonator, depicted in Figure 5.9, was fabricated with a minimum width dimension of 0.6 mm and a split dimension of 1.2 mm to demonstrate miniaturization. Besides, to adjust the resonator's resonance frequency, we increased the one-side length to 5.8 mm, as a longer length increases inductance.

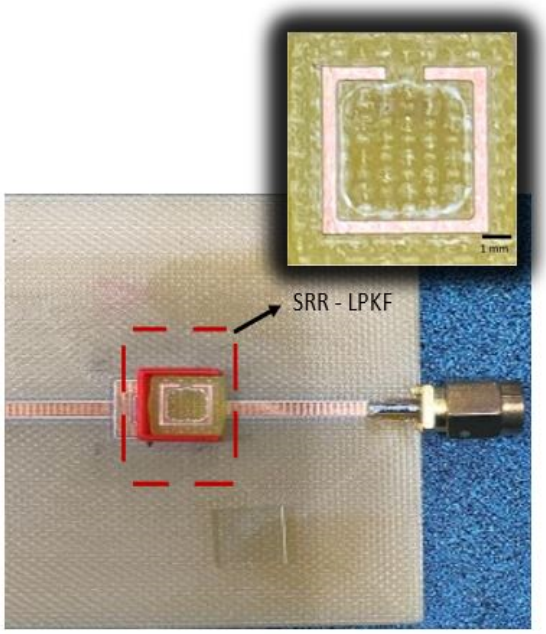

Figure 5.9: Conventional RF metamaterial resonator fabricated by the PCB milling and prototyping machine. (Scale bar: 1 mm).

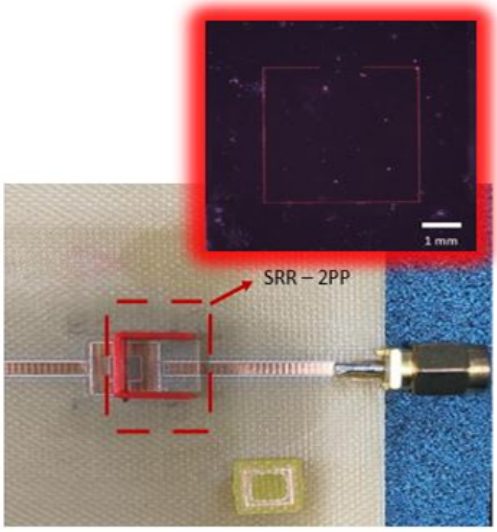

Figure 5.10: Our high-aspect ratio resonator fabricated by our proposed fabrication methods with 2PP. (Scale bar: 1 mm).

The resonance frequency decreases when the metal width of the resonator is reduced from 0.6 mm to sub-10 µm while the aspect ratio remains constant. However, the Q-factor of the resonator was also decreasing in this case. Because of that, we could not get resonance frequency. To compensate for this situation, the Q-factor can be boosted with the help of high aspect ratio metal structures. Thus, increasing the aspect ratio of the resonator is required to observe resonance frequency for sub-10 µm cases by increasing the metal thickness.

In addition, analyzing metal footprints is also essential for circuit implementation in structures with a limited area to get a similar resonance frequency with the same range Q- factor. RF metastructure resonator, having the deep third-dimension effect, acquired the same resonance frequency range of 5 GHz with a better-quality factor when the width of the metal part diminished from 0.6 mm to sub-10 µm as illustrated in Figure 5.11 (a) and Figure 5.11 (b). Here, although the length of one side of the SRR-LPKF was 5.8 mm, one side of the square RF metastructure was 4.3 mm. The findings revealed that RF metastructures using 3D printing have small metal device footprints. It means that the resonator's footprint was reduced from 33.64 mm^2 to 18.49 mm^2, a reduction of 45%.

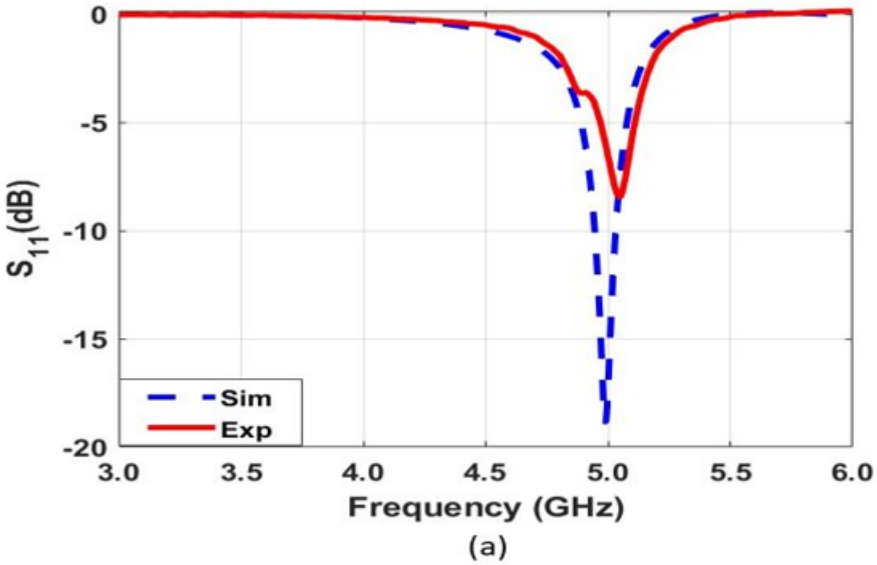

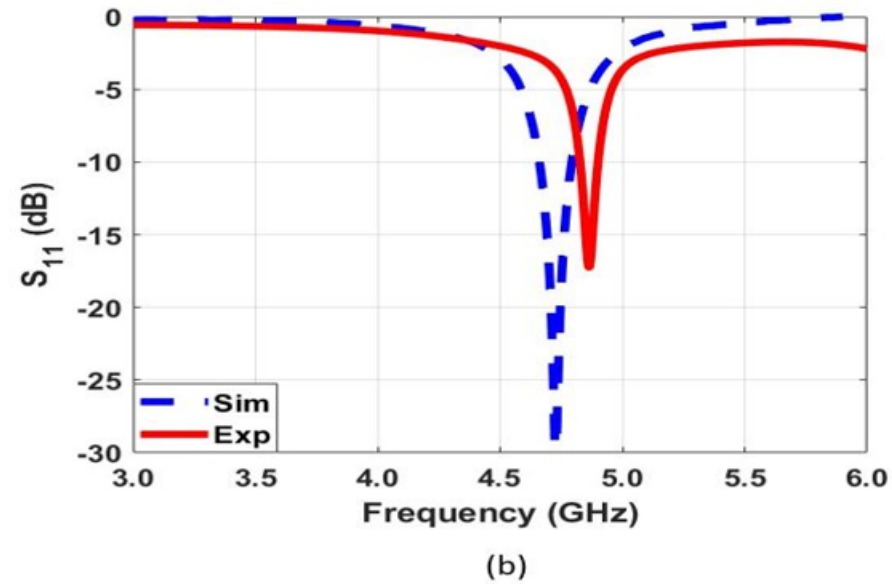

Figure 5.11: S_{11} spectra experimentally measured and numerically calculated for (a) the RF metastructure resonator fabricated by the PCB LPKF machine and (b) our RF metastructure resonator fabricated by our proposed method. These result show that the length of the resonator decreases from 5.8 mm to 4.3 mm, and the metal width decreases from 0.6 mm to sub-10 µm while increasing the aspect ratio to keep the same resonance frequency range and quality factor.

Chapter 6

Conclusion and Outlook

We have demonstrated the proposed fabrication method by combining a 3D printing system based on 2PP with electroplating for thick film metal deposition and dry etching for the seed layers. 2PP provided us with the ability to define high aspect ratio patterns with deep trenches. Electroplating allowed for metal film deposition through the deep trenches, and the dry etching process helped to have only a patterned copper conductive layer over the substrate. Here, other microfabrication methods, such as rapid thermal annealing to improve conductivity and enhance copper atom bonding, were also used.

Using the developed process flow, we fabricated a new class of high aspect ratio RF metastructure resonators utilizing the depth effect as the third dimension. Numerical solutions showed us the importance of finite metal thickness in the design procedure. Here, we designed proof-of-concept models with the desired geometrical dimensions using numerical analyses. After finishing the design of RF metastructures, we considered measurement setups to characterize these resonators to compare the experimental and numerical results. Thus, we also implemented a microstrip ring to use as an antenna while measuring. The experimental results of the fabricated RF resonators were compared with those of the numerical analysis, demonstrating that the process flow works well and the experimental results are in agreement with the numerical ones.

The effect of the metal thickness was analyzed to observe Q-factor, resonance frequency, and dimension size changes. The proposed process flow is used to miniaturize footprint size, increase the quality factor, and tune the resonance frequency in 3D RF metastructures. As a result, the findings of our experiments indicate that the method we proposed, involving the creation of deep trenches through 3D printing, presents a promising avenue for the fabrication of intricate metal-based structures with high aspect ratios.

As the future direction, this process flow will provide opportunities to create new complex designs needing high aspect ratio or 3D capability. In the metal plating part of the process flow, we especially prefer the electroplating method for metal deposition, which gives us flexibility in the design. For example, this enables the construction of metamaterials in spiral or chiral shapes. With its 3D design capability, creating inductance and capacitance effects in RF structures becomes much easier. In this case, this allows a designer to tune their specifications using process flow. Moreover, the etching mechanism is essential in terms of reproducibility and controllability for a designer. Using this process flow, a designer can keep up with isotropy-anisotropy moderation using dry etching mechanism by combining chemical etching contributing to anisotropy and physical etching contributing to isotropy. Additionally, this process flow can be combined with wet etching and is valuable in some design specifications where dry etching cannot be used.

Bibliography

[1] M. Göppert-Mayer, "Elementary processes with two quantum transitions," Annalen der Physik, vol. 18, no. 7–8, pp. 466–479, 2009.

[2] S. Maruo, O. Nakamura, and S. Kawata, "Three-dimensional microfabrication with two-photon-absorbed photopolymerization," Optics Letters, vol. 22, no. 2, p. 132, 1997.

[3] X. Zhou, Y. Hou, and J. Lin, "A review on the processing accuracy of two-photon polymerization," AIP Advances, vol. 5, no. 3, p. 030701, 2015.

[4] K. J. Schafer et al., "Two-photon absorption cross-sections of common photoinitiators," Journal of Photochemistry and Photobiology A: Chemistry, vol. 162, no. 2–3, pp. 497–502, 2004.

[5] K.-S. Lee, R. H. Kim, D.-Y. Yang, and S. H. Park, "Advances in 3D Nano/microfabrication using two-photon initiated polymerization," Progress in Polymer Science, vol. 33, no. 6, pp. 631–681, 2008.

[6] M. Rumi and J. W. Perry, "Two-photon absorption: An overview of measurements and principles," Advances in Optics and Photonics, vol. 2, no. 4, p. 451, 2010.

[7] R. L. Sutherland, Handbook of Nonlinear Optics. New York Marcel Dekker, 1996.

[8] L. Li and J. T. Fourkas, "Multiphoton polymerization," Materials Today, vol. 10, no. 6, pp. 30–37, 2007.

[9] M. Carlotti and V. Mattoli, "Functional materials for two-photon polymerization in microfabrication," Small, vol. 15, no. 40, p. 1902687, 2019.

[10] I. Sakellari et al., "3D chiral plasmonic metamaterials fabricated by direct laser writing: The twisted omega particle," Advanced Optical Materials, vol. 5, no. 16, p. 1700200, 2017.

[11] J. K. Gansel et al., "Gold helix photonic metamaterial as broadband circular polarizer," Science, vol. 325, no. 5947, pp. 1513–1515, 2009.

[12] G. Kumi, C. O. Yanez, K. D. Belfield, and J. T. Fourkas, "High-speed multiphoton absorption polymerization: Fabrication of microfluidic channels with arbitrary cross-sections and high aspect ratios," Lab on a Chip, vol. 10, no. 8, p. 1057, 2010.

[13] J. B. Reeves et al., "Tunable Infrared Metasurface on a soft polymer scaffold," Nano Letters, vol. 18, no. 5, pp. 2802–2806, 2018.

[14] M. Huff, "Recent advances in reactive ion etching and applications of high-aspect-ratio microfabrication," Micromachines, vol. 12, no. 8, p. 991, 2021.

[15] S. Gorelick, V. A. Guzenko, J. Vila-Comamala, and C. David, "Direct e-beam writing of dense and high aspect ratio nanostructures in thick layers of PMMA for electroplating," Nanotechnology, vol. 21, no. 29, p. 295303, 2010.

[16] M. A. Mohammad, S. K. Dew, and M. Stepanova, "SML resist processing for high-aspect-ratio and high-sensitivity electron beam lithography," Nanoscale Research Letters, vol. 8, no. 1, 2013.

[17] C. Luo, Y. Li, and S. Susumu, "Fabrication of high aspect ratio subwavelength gratings based on X-ray lithography and electron beam lithography," Optics & Laser Technology, vol. 44, no. 6, pp. 1649–1653, 2012.

[18] G. Karbasian et al., "High aspect ratio features in poly(methylglutarimide) using electron beam lithography and solvent developers," Journal of Vacuum Science & Technology B, Nanotechnology and Microelectronics: Materials, Processing, Measurement, and Phenomena, vol. 30, no. 6, 2012.

[19] T. N. Lo et al., "E-beam lithography and electrodeposition fabrication of thick nanostructured devices," Journal of Physics D: Applied Physics, vol. 40, no. 10, pp. 3172–3176, 2007.

[20] S. Guo et al., "Fabrication of superconducting niobium nitride nanowire with high aspect ratio for X-ray photon detection," Scientific Reports, vol. 10, no. 1, 2020.

[21] B. Päivänranta et al., "High aspect ratio plasmonic nanostructures for sensing applications," ACS Nano, vol. 5, no. 8, pp. 6374–6382, 2011.

[22] T. Konishi, H. Kikuta, H. Kawata, and Y. Hirai, "Multi-layered resist process in nanoimprint lithography for high aspect ratio pattern," Microelectronic Engineering, vol. 83, no. 4–9, pp. 869–872, 2006.

[23] Y. H. Cho et al., "Fabrication of high-aspect-ratio polymer nanochannels using a novel Si nanoimprint mold and solvent-assisted sealing," Microfluidics and Nanofluidics, vol. 9, no. 2–3, pp. 163–170, 2009.

[24] M. Brunet, T. O'Donnell, J. O'Brien, P. McCloskey, and S. C. Mathuna, "Thick photoresist development for the fabrication of high aspect ratio magnetic coils," Journal of Micromechanics and Microengineering, vol. 12, no. 4, pp. 444–449, 2002.

[25] K. S. Kim, Kyoung Nam Lee, and Y. Roh, "Formation of nanometer-scale structures using conventional optical lithography," Thin Solid Films, vol. 516, no. 7, pp. 1489–1492, 2008.

[26] V. G. Veselago, "The electrodynamics of substances with simultaneously negative values of ϵ and μ," Soviet Physics Uspekhi, vol. 10, no. 4, pp. 509–514, 1968.

[27] J. B. Pendry, A. J. Holden, D. J. Robbins, and W. J. Stewart, "Magnetism from conductors and enhanced nonlinear phenomena," IEEE Transactions on Microwave Theory and Techniques, vol. 47, no. 11, pp. 2075–2084, 1999.

[28] D. R. Smith and N. Kroll, "Negative refractive index in left-handed materials," Physical Review Letters, vol. 85, no. 14, pp. 2933–2936, 2000.

[29] J. B. Pendry, A. J. Holden, D. J. Robbins, and W. J. Stewart, "Magnetism from conductors and enhanced nonlinear phenomena," IEEE Transactions on Microwave Theory and Techniques, vol. 47, no. 11, pp. 2075–2084, 1999.

[30] W. Cai and V. M. Shalaev, Optical metamaterials: Fundamentals and applications. Cham: Springer, 2016.

[31] S. Zouhdi, Advances in Electromagnetics of Complex Media and Metamaterials. Dordrecht: Kluwer Academic Publishers, 2003.

[32] J. Fan et al., "A review of additive manufacturing of metamaterials and developing trends," Materials Today, vol. 50, pp. 303–328, 2021.

[33] R. Melik, E. Unal, N. Kosku Perkgoz, C. Puttlitz, and H. V. Demir, "Flexible metamaterials for wireless strain sensing," Applied Physics Letters, vol. 95, no. 18, p. 181105, 2009.

[34] R. Melik et al., "Nested metamaterials for wireless strain sensing," IEEE Journal of Selected Topics in Quantum Electronics, vol. 16, no. 2, pp. 450–458, 2010.

[35] S. Gokyar, A. Alipour, E. Unal, E. Atalar, and H. V. Demir, "Wireless deep-subwavelength metamaterial enabling sub-mm resolution magnetic resonance imaging," Sensors and Actuators A: Physical, vol. 274, pp. 211–219, 2018.

[36] J. M. Drozd and W. T. Joines, "Determining Q using s parameter data," IEEE Transactions on Microwave Theory and Techniques, vol. 44, no. 11, pp. 2123–2127, 1996.

[37] T. A. Ameel, R. O. Warrington, R. S. Wegeng, and M. K. Drost, "Miniaturization Technologies applied to energy systems," Energy Conversion and Management, vol. 38, no. 10–13, pp. 969–982, 1997.

[38] A. Vallecchi, E. Shamonina, and C. J. Stevens, "Analytical model of the fundamental mode of 3D Square split ring resonators," Journal of Applied Physics, vol. 125, no. 1, p. 014901, 2019.

[39] O. Sydoruk, E. Tatartschuk, E. Shamonina, and L. Solymar, "Analytical formulation for the resonant frequency of Split Rings," Journal of Applied Physics, vol. 105, no. 1, p. 014903, 2009.

[40] S. K. Samanta, R. Pradhan, and D. Syam, "Theoretical approach to verify the resonance frequency of a square split ring resonator," Journal of the Optical Society of America B, vol. 38, no. 10, p. 2887, 2021.

[41] Md. R. Islam et al., "Metamaterial based on an inverse double V loaded complementary square split ring resonator for radar and Wi-Fi Applications," Scientific Reports, vol. 11, no. 1, 2021.

[42] F. Iza and J. A. Hopwood, "Low-power microwave plasma source based on a microstrip split-ring resonator," IEEE Transactions on Plasma Science, vol. 31, no. 4, pp. 782–787, 2003.

[43] A. Bogner et al., "Planar microstrip ring resonators for microwave-based gas sensing: Design aspects and initial transducers for humidity and ammonia sensing," Sensors, vol. 17, no. 10, p. 2422, 2017.

[44] P. Dixit and J. Miao, "Aspect-ratio-dependent copper electrodeposition technique for very high aspect-ratio through-hole plating," Journal of The Electrochemical Society, vol. 153, no. 6, 2006.

[45] J. D. Plummer, M. D. Deal, and P. B. Griffin, "Etching," in Silicon Vlsi Technology: Fundamentals, Practice and Modeling, India: Pearson India Education Services, 2016.

[46] H.-S. Kim, J.-C. Woo, Y.-H. Joo, and C.-I. Kim, "A study of the surface reaction on the etched ito thin films by using inductively coupled plasma," Vacuum, vol. 93, pp. 7–12, 2013.